Study on the Effect of Process Parameters of Laser Powder Bed Fusion on the Microstructure and Mechanical Properties of SAF 2507 Super Duplex Stainless Steel

ANISUL ISLAM SUVA

SUPERVISOR
Foysal Kabir Tareq
Geir Grasmo
Souman Rudra
Kazi Afzalur Rahman

University of Agder, [2024]
Faculty of Engineering and Science
Department of Engineering Sciences

Master

Abstract

Laser-powder bed fusion (L-PBF) is a type of additive manufacturing (AM) that involves the addition of metal powders in a sequential layer-by-layer manner to create near-net-shape components. An outstanding characteristic of this technology is its ability to achieve high cooling rates, reaching up to 10^7 K/s. This unique characteristic has benefits in the production of high-strength stainless steel alloys, as it helps to reduce unwanted phase formation. SAF 2507 super duplex stainless steel (SAF 2507 SDSS), a type of stainless-steel alloy, contains around 25% chromium and 7% nickel, has a unique phase composition with an equal distribution of about 50% ferrite and 50% austenite and characterized by its higher mechanical strength and resistance to corrosion, which are attributed to its high levels of chromium and nickel content along with its low level of carbon. Producing intricate geometry with SAF 2507 using traditional methods with a specific phase composition is challenging and requires post-processing. LPBF is an alternative technology capable of manufacturing near-net-shape components with complicated geometry. It is important to conduct a comprehensive investigation to retain the desired phase composition while fabricating components using L-PBF. Although several studies have investigated the microstructure and mechanical properties of SAF 2507 using L-PBF. However, the influence of different L-PBF process parameters as well as energy density on microstructure and mechanical properties has yet to be investigated. This study examines the influence of L-PBF process parameters (laser power, scan speed, hatch distance) on the microstructure and mechanical properties of SAF 2507 SDSS. Additionally, the corrosion properties are investigated using the established optimum parameters. A design of experiment (DoE) was performed using the central composite design over a wide range of process parameters: laser power (100–300 W), scan speed (250–1000 mm/s), and hatch distance (50–180 µm) to investigate their effect on the microstructural and mechanical properties of SAF 2507. By implementing the selected parameter set, the as-built SAF 2507 SDSS sample had porosity less than 1%, a Vicker hardness ranging from 288 to 357 HV, a yield strength of 824 to 1220 MPa, an ultimate tensile strength of 965 to 1304 MPa, elongation of 6% to 18.1%, and a corrosion rate of 127.65 µm/y was determined. The findings derived from this investigation have the potential to facilitate the customization of component quality by meeting design specifications and minimizing as-built defects, thereby decreasing the need for post-processing.

Abstrakt

Laser-powder bed fusion (L-PBF) er en type additiv produksjon (AM) som involverer tilsetning av metallpulver på en sekvensiell lag-for-lag-måte for å lage komponenter i nesten nettform. Et enestående kjennetegn ved denne teknologien er dens evne til å oppnå høye kjølehastigheter, som når opp til 10^7 K/s. Denne unike egenskapen har fordeler ved produksjon av høyfaste rustfrie stållegeringer, da den bidrar til å redusere uønsket fasedannelse. SAF 2507 super duplex rustfritt stål (SAF 2507 SDSS), en type rustfri stållegering, inneholder rundt 25 % krom og 7 % nikkel, har en unik fasesammensetning med en lik fordeling på ca. 50 % ferritt og 50 % austenitt, og er preget av sin høyere mekaniske styrke og motstand mot korrosjon, noe som tilskrives dets høye nivåer av krom- og nikkelinnhold sammen med det lave nivået av karbon. Å produsere intrikat geometri med SAF 2507 ved bruk av tradisjonelle metoder med en spesifikk fasesammensetning er utfordrende og krever etterbehandling. LPBF er en alternativ teknologi som er i stand til å produsere nesten-nettformede komponenter med komplisert geometri. Likevel er det nødvendig å gjennomføre en omfattende studie for å beholde den ønskede fasesammensetningen mens man fremstiller komponenter ved bruk av L-PBF. Flere studier har undersøkt mikrostrukturen og de mekaniske egenskapene til SAF 2507 ved bruk av L-PBF. Denne studien undersøker påvirkningen av L-PBF-prosessparametere (laserkraft, skannehastighet, skraveringsavstand) på mikrostrukturen og de mekaniske egenskapene til SAF 2507 SDSS. I tillegg blir korrosjonsegenskapene undersøkt ved å bruke de etablerte optimale parameterne. Et eksperimentdesign (DoE) ble utført ved bruk av den sentrale kompositttdesignen over et bredt spekter av prosessparametere: lasereffekt (100–300 W), skannehastighet (250–1000 mm/s) og skraveringsavstand (50–180 µm)) for å undersøke deres effekt på de mikrostrukturelle og mekaniske egenskapene til SAF 2507. Ved å implementere det valgte parametersettet hadde SAF 2507 SDSS-prøven som er bygget porøsitet mindre enn 1 %, en Vickers-hardhet som varierer fra 288 til 357 HV, en flytegrense på 824 til 1220 MPa, en strekkfasthet på 965 til 1305 MPa, forlengelse på 6% til 18,1% og en korrosjonshastighet på 127,65 µm/år ble bestemt. Funnene fra denne undersøkelsen har potensial til å lette tilpasningen av komponentkvalitet ved å møte designspesifikasjoner og minimere as-built-defekter, og dermed redusere behovet for etterbehandling.

Preface

This thesis work was conducted under the project "Collaborative Action for Improving Educational Capacities in Renewable Energy to mitigate climate crisis (CARE)" between Chittagong University of Engineering & Technology (CUET), Bangladesh and University of Agder (UIA), Norway (Collaboration Agreement No. NORPART-2021/10355).

I would like to express my sincere gratitude to my supervisors, Foysal Kabir Tareq, Geir Grasmo, and Souman Rudra, for their excellent guidance, supervision, and valuable advice throughout the project. I am also grateful to Prof. Kazi Afzalur Rahman, CUET, for his motivation and mentorship during my thesis work.

I want to express my gratitude to Cecilie Ødegård, and Harald Sauvik from the University of Agder, and Mechatronics Innovation Lab AS, who assisted me in completing the M.Sc. thesis.

I want to express my deepest gratitude to my deceased father, Md. Rafiqul Islam, my mother, my wife, and my sisters for their unwavering assistance and encouragement during my educational pursuit. Devoid of their assistance, I would have been unable to attain this stage.

I want to express my heartfelt appreciation to everyone for their assistance with technical matters and their moral encouragement and helpful advice in the thesis work.

Anisul Islam Suva
University of Agder, Norway
Grimstad, February 2024

Individual/group Mandatory Declaration

The individual student or group of students is responsible for the use of legal tools, guidelines for using these and rules on source usage. The statement will make the students aware of their responsibilities and the consequences of cheating. Missing statement does not release students from their responsibility.

1.	I/We hereby declare that my/our report is my/our own work and that I/We have not used any other sources or have received any other help than mentioned in the thesis.	☒
2.	I/we further declare that this thesis: - has not been used for another exam at another department/university/university college in Norway or abroad; - does not refer to the work of others without it being stated; - does not refer to own previous work without it being stated; - have all the references given in the literature list; - is not a copy, duplicate or copy of another's work or manuscript.	☒
3.	I/we am/are aware that violation of the above is regarded as cheating and may result in cancellation of exams and exclusion from universities and colleges in Norway, see Universitets- og høgskoleloven §§4-7 og 4-8 og Forskrift om eksamen §§ 31.	☒
4.	I/we am/are aware that all submitted theses may be checked for plagiarism.	☒
5.	I/we am/are aware that the University of Agder will deal with all cases where there is suspicion of cheating according to the university's guidelines for dealing with cases of cheating.	☒
6.	I/we have incorporated the rules and guidelines in the use of sources and references on the library's web pages.	☒

UiA University of Agder Norway

Publishing Agreement

Authorization for electronic publishing of the thesis.

Author(s) have copyrights of the thesis. This means, among other things, the exclusive right to make the work available to the general public (Åndsverkloven. §2).

All theses that fulfill the criteria will be registered and published in Brage Aura and on UiA's web pages with author's approval.

Theses that are not public or are confidential will not be published.

I hereby give the University of Agder a free right to

make the task available for electronic publishing: ☒JA ☐NEI

Is the thesis confidential? ☐JA ☒NEI

(confidential agreement must be completed and signed by the Head of the Department)

- If yes:

Can the thesis be published when the confidentiality period is over? ☐JA ☐NEI

Is the task except for public disclosure? ☐JA ☒NEI

(contains confidential information. see Offl. §13/Fvl. §13)

Contents

List of Figures

List of Tables

Notation

P	Laser power(w)
SS	Scan speed
HD	Hatch distance
LT	Layer thickness

Abbreviations

AM	Additive Manufacturing
LPBF	Laser Powder Bed Fusion
SLM	Selective Laser Melting
SDSS	Super Duplex Stainless Steel
DSS	Duplex Stainless Steel
SAF 2507	SAF 2507 super duplex stainless steel
EN	European Number
SEM	Scanning Electron Microscope
LOM	Light Optical Microscope
ASTM	American Society for Testing and Materials
PREN	Pitting Resistance Equivalent Number
FCC	Face Centric Cubic
BCC	Body Centric Cubic
APF	Atomic Packing Factor

Chapter 1

Introduction

1.1. Background

The Additive Manufacturing (AM) sector is noticing rapid growth, with an increasing number of markets exploring the potential applications of this technology [1]. These days, business and academics are paying attention to metallic materials that are made by AM [2]. The ability to build items quickly, effectively, and securely in the desired geometry and with the corresponding mechanical qualities makes it possible to implement a digital spare parts warehouse in the form of computer-generated models. By doing this, it becomes possible to decrease and even completely do away with the requirement to have spare parts on hand in favour of being able to generate the required parts as needed [3]. Prototypes and customized parts can also be produced more quickly and effectively than using traditional processes. This technology can be applied because it is capable of reproducing items with the required shape and expected mechanical qualities.
Laser powder bed fusion (LPBF) is a form of AM that involves the layer-wise addition and consolidation of metal powders in near-net-shape parts. LPBF technology is being used more often to produce items with complex shapes at a reasonable cost for a range of important applications [4]. Research and investigations into LPBF techniques and equipment are being conducted with the goal of producing materials with the most faithful qualities possible, making the procedure more useful both practically and economically [5]. From the time of its invention LPBF metals has transitioned from prototyping technology into a multi-billion-dollar manufacturing revolution [6][7]. Design integration, reductions in lead times, ability to manufacture hard metals, novel properties of as-printed parts, defect rectification, recycling of the spent powders, ability to function with almost zero waste generation are some of the advantages AM offers over subtractive manufacturing [8]. The LPBF technique is characterized by high cooling rates, reaching up to 10^7 K/s, which effectively prevents undesired phase development in metal alloy [9][10]. This unique characteristic has benefits in the production of high-strength stainless steel alloys as it prevents unwanted phase formation in this alloy. In addition, the process of printing stainless steel alloys using LPBF requires a lower laser energy density to form the melt pool and fabricate the components for their lower thermal conductivity and higher laser absorption capacity compared to other alloys [11].

Among the stainless steels, SAF 2507 Super duplex stainless steel (SAF 2507) is known for its excellent combination of corrosion resistance and high strength. The microstructure consists of two phases with nearly equal composition of approximately 50% ferrite & 50% austenite [12]. Super duplex stainless steel (SDSS) is an alloy of approximately 25% Cr, 7% Ni, 0.3% Mo, 0.2% N that was developed during the early part of the 21st century. This specific composition has also been standardized by ASTM under the designation UNS 32750 [13] [14]. Notable about SAF 2507

SDSS is that it has roughly twice the strength of more conventional stainless steels (304, 316L) while improving their corrosion characteristics [10]. SDSS often has a higher resistance to pitting corrosion than the conventional 300 series [15]. This is due to the chemical composition, specifically the chromium component [16]. SDSS is particularly resistant to stress corrosion cracking (SCC) due to its high strength and outstanding corrosion resistance [17]. Because they use less material due to their high strength, they can also be less expensive [18]. Even though duplex stainless steel (DSS) has been around since the 1930s, researchers are constantly searching for new ways to innovate, such finding different ways to produce duplex stainless steel [19]. Because of the high strength and resistance to corrosion, super duplex stainless steels are extensively utilized in petrochemical, oil, and gas, shipping, and other industries. These exceptional qualities are ensured by the appropriate 50/50 austenite to ferrite phase balance [20]. However, exact thermomechanical processing of DSS-wrought products has increased expenses [21]. Examining appropriate production procedures is therefore crucial for the creation of SDSS structural components. Compared to other forms of stainless steel, SDSS is more challenging to process, and the SLM procedure has not yet been sufficiently improved for this class of materials [22]. Due to the growing demand for 3D-printed SDSS, companies are seeking to advance and enhance the SLM method for this type of materials [23].

The production of iron-based metal parts using LPBF has a well-established history in literature and industry, particularly for standard grade stainless steels including martensitic, austenitic, and ferritic steels [24][25][26][27]. Very few investigations on the LPBF fabrication of duplex stainless steels have been performed and reported. These studies looked at the changes in the mechanical properties and microstructure of the SAF 2507(SDSS) that were processed using LPBF [28][29][30]. Previous investigation showed that in as-printed samples, ferrite was the main phase, whereas in heat-treated samples, the duplex structure was found. Additionally, the investigations showed that, in comparison to heat-treated samples, as-printed samples showed extremely high strength and little elongation [31]. The microstructure evolution in the LPBF manufacturing of gas atomized SDSS powders was studied by Davidson et al. [32] and found that ferrite is the common phase in the printed samples with austenite precipitating at the grain boundaries or forming Widmanstätten laths, the ferrite grains were elongated in the build direction. In similar investigations, also showed that ferrite was the primary phase in higher energy density in the microstructure of the gas-atomized 25Cr7Ni LPBF processing [33][34]. Very few investigations on the LPBF process parameters on microstructure and mechanical properties of duplex stainless steels have been performed and reported. Additionally, few research was done to characterize the corrosion properties with parameters that were manufactured using LPBF. These subjects are the focus of the current investigation. The primary goal of the study is to investigate the effects of process parameters on microstructure, mechanical, and corrosion behaviours of gas-atomized SAF 2507 that was manufactured using L-PBF. The research results will help in selecting the range of process parameters to get desired output of microstructural, mechanical and corrosion properties using LPBF technology. The results will also help to clarify how changing of LPBF process parameters affect the microstructural, mechanical and corrosion properties of the printed samples.

1.2. Aims and objectives.

This research aims to study the influence of LPBF process parameters on the microstructure and mechanical properties of SAF 2507 (EN 1.4410). This aim will be achieved through the following objectives**:**

1. Selecting parameter ranges using DoE.
2. Effect of different process parameters on microstructural and phases
3. Effect of different process parameters on mechanical properties
4. Evaluation of corrosion behaviour SLM printed parts.
5. Compare the results with standards.

1.3. Research Questions

The primary question of this thesis is- How do the LPBF process parameters influence the microstructure and mechanical properties of SAF 2507? In addressing this primary question, the thesis aims to answer the following research inquiries.

1. How can a set of parameters for generating samples be obtained?
2. How do the parameters of the LPBF process affect the porosity of as-built samples?
3. How do the parameters of the LPBF process influence the microstructure of as-built samples?
4. What is the impact of LPBF process parameters on the microhardness of as-built samples?
5. What is the impact of LPBF process parameters on the ultimate tensile strength, yield strength, and elongation of as-built samples?
6. What is the corrosion rate associated with the energy density that produces minimum porosity?

1.4 Thesis Outline

This thesis consists of five chapter.

Chapter 1: Presents an introduction and background information on the selected problem and the objectives of this research followed by Research questions.

Chapter 2: Presents a comprehensive analysis of the existing literature and theoretical framework, providing a deep insight into additive manufacturing (AM), its categorization, selective laser melting (SLM), and different process parameters of laser power bed fusion, and concludes with an overview of super duplex stainless steel.

Chapter 3: Outlines the methodology, manufacturing methods, and characterization procedures used for the samples.

Chapter 4: Provides an analysis of the impact of LPBF process parameters on porosity, microstructure, tensile strength, and elongation. The chapter concludes by examining the corrosion rate, focusing on the sample with the lowest porosity.

Chapter 5: Provides a concise summary of our findings and proposes more research opportunities.

Chapter 2

Theoretical background

2.1 Additive Manufacturing (AM)

Additive manufacturing methods have the capacity to produce a diverse range of materials, including ceramics, glass, metals, polymers, and composite materials. According to ASTM guidelines, the range of additive manufacturing techniques is categorized into various groups (Fig 1), which include selective laser melting (SLM), stereolithography (SLA), selective laser sintering (SLS), electron beam melting (EBM), direct energy deposition, sheet lamination, material extrusion, and vat photo-polymerization [35], [36]. Within each category, there are several distinct techniques, but all are based on the same principle: the selective modelling of layers. Due to the stacking of layers, the parts produced by AM methods exhibit some anisotropy in one direction. Anisotropy can be decreased by selecting the proper orientation during the part's production. Materials used for AM can range from polymers and ceramics to metals and composites, depending on the kind of AM process being used. The following are some of the main AM techniques with promising applications in Engineering, Construction, Medical, Military, Aeronautics, Fashion, Architecture, Computer Industry.

2.2 Classification of AM

Additive manufacturing (AM) classification generally entails grouping different methodologies according to their fundamental input, working methods, and materials.

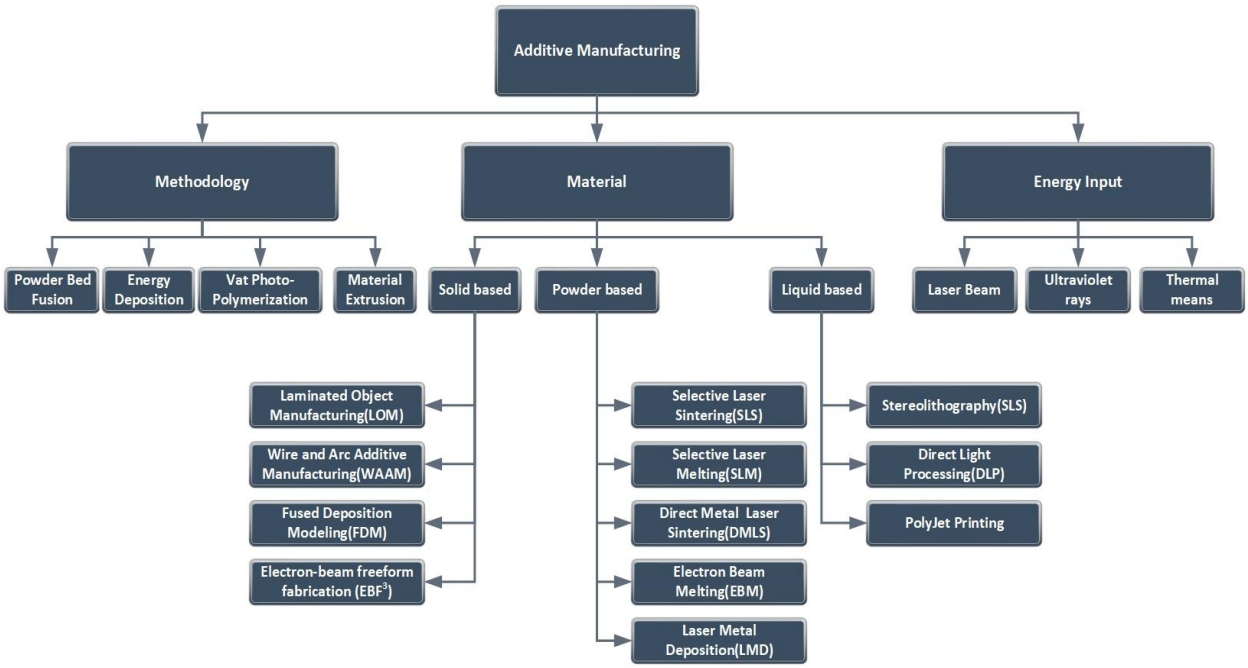

Figure 1. Classification of additive manufacturing processes from different contexts [36].

2.2.1. Powder bed fusion

Power bed fusion (PBF) is an additive manufacturing process in which thermal sources (e.g. lasers or electron beams) are used to fuse the powder particles in a consistent manner to construct structures using computer-aided design.

The following are examples of types of Powder bed fusion (PBF) processes:

1. Selective Laser Sintering (SLS)
2. Selective Laser Melting (SLM)
3. Direct Metal Laser Sintering (DMLS)
4. Selective Heat Sintering (SHS)
5. Electron Beam Melting (EBM)

2.2.1.1 Selective laser melting (SLM)

Selective laser melting (SLM) is an additive manufacturing process where a high-density laser beam scans a powder bed, melting solidified layers to create a functional three-dimensional part or prototype [37]. It melts alloy powder particles instead of sintering [38]. Germany initially adopted this method in 1999. The technology was developed by Fockele and Schwarze (F&S) in collaboration with the Fraunhofer Institute of Laser Technology. The SLM technique constructs goods by using high-energy laser beams on a powder bed, layer by layer. Currently, it is a highly favoured technique to produce metal components. SLM utilizes a laser mounted on the upper part, accompanied by a series of lenses that concentrate on the powdered material to achieve solidification of the layer, as seen in Figure 2. After each layer is fused together, the construction platform descends, and the recoating arm applies a new layer on top of the previous one. This

sequence continues until the entire part is fully formed. The layer of powder must have a minimum thickness of 0.020 mm [39].

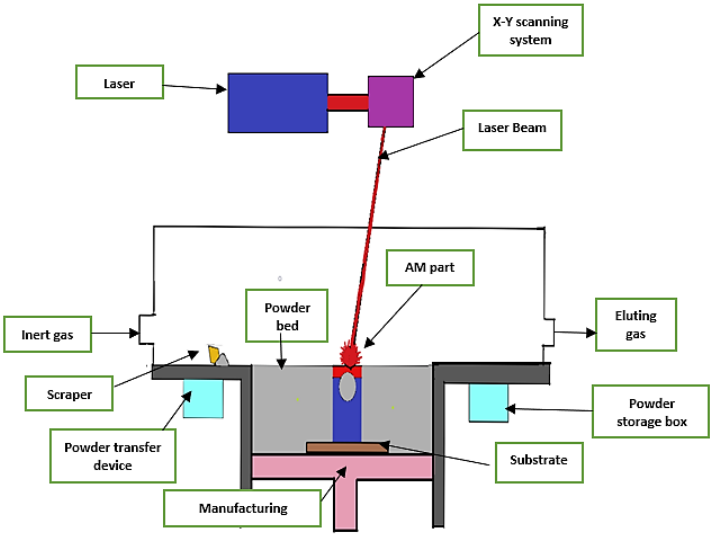

Figure 2. Schematic Diagram of Selective Laser Melting Process (SLM) [39]

In recent times, high-intensity lasers have been incorporated into Selective Laser Melting (SLM) technology, with the advancements in fibre optics. This integration allows for the processing of many metallic materials, including tungsten, copper, and aluminium. Hence, a wide range of metallic materials can undergo the process of melting on Selective Laser Melting (SLM). This facilitated the development of several research possibilities in the field of SLM for composite and metallic materials. This method of production offers the benefits of generating goods with excellent precision and superior quality [39]. SLM components have exceptional mechanical characteristics. SLM is utilized to produce components in the aerospace, automotive, and medical industries. The production of a lattice structure can be achieved by the process of Selective Laser Melting. Deficiencies can be detected and assessed [40]. A microbial fuel cell is a device that harnesses the power of microorganisms to generate electricity from renewable resources or waste products. The technique of Selective Laser Melting (SLM) was utilized to manufacture the essential elements of Microbial Fuel Cells (MFCs), such as a bio-inspired lattice aluminium alloy anode and a 3D macro-porous structure. These components possess a high specific surface area and surface roughness, which are ideal for accommodating microorganisms and enhancing power efficiency. The optimal energy recovery rate was around 3 kWh/m^3 per day [41]. SLM possesses a very varied process capability, enabling it to manufacture new components, restore and reconstruct old or damaged components, and provide protective coatings that resist wear and corrosion [42].

2.3 Process parameters of SLM

Several parameters can influence LPBF procedures used in additive AM to create components. A portion of these parameters is used to ascertain the energy density administered to the powder layer in the LPBF procedure.

$$E_d = \frac{P}{V_s * D_h * T_l} \quad \text{..... equation 1}$$

The variables in the equation are as follows: E_d is the energy density (J/mm^3), P is the laser beam power (W), Vs is the laser scan speed (mm/s), D_h is the hatch spacing between scan passes, and T_l is the deposited layer thickness (µm).

It is essential to examine the correlation between process parameters and the mechanical and material characteristics of a SAF 2507 produced using laser powder bed fusion. This investigation will focus on three process parameters: laser power, hatch distance, scan speed, as well as the total laser energy density.

2.3.1 Laser Power

The laser power directly influences the quantity of energy that is used to liquefy the powder layer and generate a productive molten pool. Lowering the laser intensity can lead to inadequate powder melting or reduced depth of laser penetration, which may prevent complete melting of the powder and fusion of subsequent layers. Excessive laser power can result in the evaporation of material, leading to the formation of gas bubbles and the creation of porosity in the recently melted layers of powder [42].

Yadroitsev et al. examined how energy density-related factors affect the geometric properties of individual tracks formed by melting stainless steel powder on an LPBF machine [43]. The researchers discovered that laser power had the greatest impact on the geometrical properties of a single track. Following this, the powder layer thickness, scanning speed, and powder particle size were shown to have progressively less significance. In their investigation employing stainless steel powder, Gu et al. reduced the laser power from 195 W to 70 W and dropped the scan speed from 800 mm/s to 287 mm/s, while keeping the energy density unchanged at 61 J/mm3. They also discovered that there was an increase in porosity and a decrease in density [44]. Dingal et al. enhanced the laser power in an iron powder laser sintering system and observed a decrease in porosity [45]. Abele et al. discovered that the effect of laser power on tensile strength was minimal compared to hatch distance and scan speed. However, raising the laser power from 165 W to 180 W resulted in a decrease in porosity and an increase in tensile strength of stainless steel (17-4 PH) specimens [46]. Qiu et al. discovered that raising the laser power from 150 W to 200 W led to a reduction in the porosity of titanium alloy [47].

2.3.2. Scan Speed

The scan speed, which refers to the velocity at which the laser beam moves across the powder layer to melt it, plays a crucial role in reducing the total manufacturing time for an LPBF product. Nevertheless, if the scanning velocity is excessively rapid, the laser could not possess an adequate duration to liquefy the powder. To enhance the melting process and attain equivalent energy density, one may either decrease the hatch distance or increase the laser power, which would also enable a higher scan speed. Kempen et al. discovered that by increasing the scan speed from 120 mm/s to 600 mm/s, the hardness and relative density of steel (18Ni-300) decreased [48]. According to Sun et al., the density of titanium alloy (Ti-6Al-4V) was seen to rise when the scan

speed decreased [49]. Delgado et al. conducted a comparative analysis of two additive manufacturing (AM) systems. They found that one system led to decreased hardness and ultimate tensile strength (UTS) as the scan speed rose. However, the other system did not show any notable changes in either hardness or UTS [50]. Vandenbroucke and Kruth conducted research where they adjusted the scanning speed to reduce the presence of small pores and meet the specific mechanical property criteria, such as hardness, strength, stiffness, and ductility, for titanium alloy components produced using an LPBF system [51]. The laser intensity and layer thickness remained consistent. When the scan speed was increased from 90 mm/s to 190 mm/s, the scan tracks did not entirely melt, resulting in the formation of large holes and a drop in the observed component density. Qiu et al. employed a comparable additive manufacturing (AM) technology to fabricate components made of titanium-based alloy (Ti-6Al-4V). They modified the scanning speed from 800 mm/s to 1500 mm/s [47]. The researchers discovered a negative correlation between porosity and scan speed.

Abele et al. discovered that by raising the scanning speed from 1150 mm/s to 1350 mm/s, the porosity of stainless-steel specimens increased but their tensile strength decreased [46]. Liu et al. manipulated the scan speed for powders with two distinct particle size distributions [52]. The observed component bulk density exhibited a negative correlation with the scan speed, as it decreased with higher scan speeds. The UTS system achieved its peak performance across a diverse range of scan speeds, indicating the existence of an ideal scan speed for the system. Gu et al. discovered a comparable correlation in which decreasing the scanning speed from 1200 mm/s to 600 mm/s resulted in a decrease in porosity and an increase in density of stainless-steel samples [44]. Song et al. conducted an experiment where they enhanced the scanning speed from 100 mm/s to 300 mm/s. As a result, they observed a reduction in hardness for a different nickel alloy (NiCr) [53].

2.3.3. Hatch Distance

The hatch distance/spacing refers to the distance between the centres of consecutive laser tracks as the laser beam moves over the layer of powder. Reducing the hatch distance will result in a greater degree of overlap between each laser pass, perhaps causing excessive burning around the outside border of the laser track. Augmenting the hatch distance might potentially impede the laser's ability to sufficiently overlap and thus lead to inadequate powder melting. Vandenbroucke and Kruth conducted research where they adjusted the hatch distance to reduce porosity and satisfy the mechanical property criteria for hardness, strength, stiffness, and ductility of titanium alloy components produced using an LPBF system [51]. The laser intensity and layer thickness remained consistent. The augmentation of the hatch distance from 0.12 mm to 0.14 mm led to incomplete fusion of the scan tracks, the formation of significant holes, and a reduction in density. Sun et al. used titanium alloy powder in conjunction with a bespoke LPBF system, while simultaneously modifying the hatch distance [49]. As the distance between hatches reduced, the density rose. Abele et al. investigated the impact of energy density-related factors on the porosity and mechanical characteristics of thin-walled hollow cylinders fabricated from stainless steel. They discovered that the hatch distance had the most significant influence on the tensile strength. The scan speed exhibited the second most significant influence, whereas laser power had the least significant impact on the tensile strength. The porosity was raised, and the tensile strength was lowered by increasing the hatch spacing from 0.12 mm to 0.19 mm [46].

2.3.4. Layer Thickness

Increasing the depth of the powder layer during each laser solidification step might expedite the total manufacturing time of a component. Nevertheless, if the thickness of the powder layer exceeds a certain limit, it may impede the formation of a sufficiently deep melt pool required for melting and fusing two consecutive layers. To produce the same effective melt pool, a slower scanning speed or a greater laser power is necessary when dealing with a thick coating of powder.

Kempen et al. conducted a study to assess the impact of altering the thickness of layers on the hardness and density of a specific steel alloy known as 18Ni-300 [48]. It was discovered that when the thickness of the layer rose from 0.03 mm to 0.06 mm, both hardness and relative density dropped. Sun et al. employed a specialized selective laser melting (SLM) technique to utilize titanium (Ti-6Al-4V) powder [49]. Additionally, it was discovered that the density exhibited a drop in proportion to the rise in layer thickness. Augmenting the thickness of the layers caused a rise in porosity, which subsequently led to a reduction in density of the fabricated component [54]. In their study, Dingal et al. employed iron powder on a specialized laser sintering system. They discovered that raising the thickness of the powder layer from 0.2 mm to 0.4 mm led to an augmentation in porosity, as well as a decrease in density and hardness [45]. Delgado et al. evaluated the influence of modifying the thickness of layers on two distinct additive manufacturing (AM) systems using stainless-steel powders [50]. One system exhibited a decrease in hardness as the layer thickness increased, whereas the other system showed no substantial alteration in hardness with increasing layer thickness.

2.4 Defect in SLM printed SAF 2507

Porosity is often categorized into three distinct groups: lack of fusion pores, metallurgical pores, and keyhole pores. Metallurgical pores are formed because of the presence of oxygen and other impurities, measuring 100 µm in diameter and having a spherical shape. The lack of fusion pores manifests with an elevated scanning velocity. Typically, the lack of fusion pores exhibited irregular forms larger than 100 µm, as seen in Figure 3. The development of keyhole mode pores demonstrated a progressive rise in size with power. The number and size of keyhole holes grow as the power increases. However, when the scan speed is faster, the production of keyhole pores is inhibited and only occurs at higher power levels. At greater scan speeds, the safe processing window is consequently bigger [24][25].

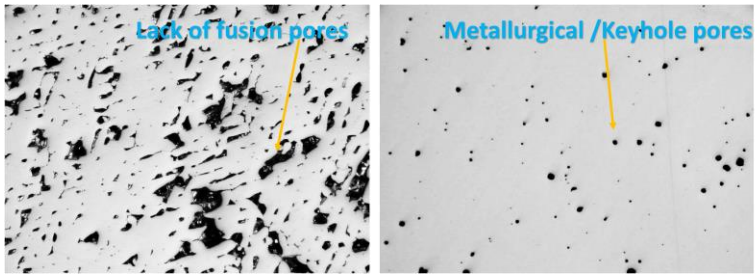

Figure 3. Different types of pores formation.

2.5 Super Alloy

Superalloys are characterized by their superior heat resistance, high levels of strength and toughness, improved dimensional stability, and rigidity retention [55],[56]. Superalloys are characterized by their superior heat resistance; high levels metal's microstructure and mechanical properties vary at high temperature. When exposed to high temperatures, such as in power plants, airplanes, oil and gas extraction, and processing units, the metal loses strength. These weaknesses in metals functioning at high temperatures can be avoided by creating an alloy that can withstand high temperatures [57]. Alloy metals are combined with wear-resistant metals to enhance their qualities, resulting in a superalloy. Superalloy materials have great temperature resistance as well as resistance to oxidation, corrosion, creeping, and abrasion [58].

Three classes can be used to generally categorize super alloys [59]. They are listed as follows: -

1. Base made of Nickel.
2. Base of Nickel-iron.
3. Base of Cobalt.

The properties of nickel-iron base superalloys, or super duplex stainless steel, are the focus of this thesis.

2.6. Duplex Stainless Steel

Ferritic (δ) and austenitic (γ) microstructures form the basic phase composition of duplex stainless steel (DSS). Once DSS steel is melted, it will solidify into a ferritic structure that is roughly 100% ferritic. A portion of the ferritic structure will turn into austenite when it cools to room temperature. The most popular and ideal kind of DSS has a ferrite to austenite ratio of almost 50/50. DSS steel will benefit from both the greater yield strength of ferrite and some of the work-hardened characteristics that result in tensile strength with such an equal distribution. The austenitic microstructure is responsible for this characteristic. Therefore, DSS steel fills the gap in the market that exists between ferritic and austenitic stainless steel [60]. DSS offers certain advantages over austenitic stainless steel, such as superior mechanical strength and anti-corrosion properties. DSS advantages over austenitic stainless steels can be increased by using it in places where typical austenitic stainless steels are inappropriate owing to stress corrosion cracking. [61].

2.6.1. Super Duplex Stainless Steel

A super duplex stainless steels composition and variety of alloying components can be used to identify it. Super Duplex is very resistant to uniform corrosion by organic acids like acetic and formic acid because of its high chromium and molybdenum content. Moreover, Super Duplex is more resilient to inorganic acids, especially those that contain chlorides. This product is specifically designed to meet the needs of the oil and gas and chemical industries, offering superior corrosion resistance and strength. For most material types, the Super Duplex pitting resistance equivalent (PREN) will be greater than 38 [62] Super-duplex chromium-nickel stainless steel with additional copper content is known as Alloy SAF 2507 (EN 1.4410 / ASTM S32750). Table 1 below displays the EN 1.4410 material's chemical composition [63], [64].

Table 1: Chemical Composition of EN 1.4410(ASTM S32750) [63], [64].

UNS Number	C	Mn	P	S	Si	Cr	Ni	Mo	N	Cu	Other
S32750	0.03	1.2	0.035	0.02	0.8	24.0-26.0	6.0-8.0	3.0-5.0	0.24-0.32	0.5	-

The physical and chemical characteristics of each alloy element are unique. Based on these features, every factor influences the superalloy's qualities. In the section below, the significance of the super duplex stainless steel alloying elements is briefly discussed.

2.7. Microstructure of Super Duplex Stainless Steel

There can be two distinct primary phases in DSS alloys. An iron-carbon alloy can be either austenitic or ferritic. The lattice structures of these phases vary, influencing the solubility and mechanical characteristics of other elements. Figure 4 describes the crystal structures of the austenite phase and the delta ferrite phase. The austenite phase has a face-centred cubic (FCC) crystal structure. An FCC structure is shown to have a higher atom than a BCC structure. For FCC and BCC, the corresponding atomic packing factors (APFs) are 0.74 and 0.68, respectively. This indicates that there is more packing inside the FCC structure. Additionally, it is evident that the FCC and BCC have different coordination numbers—that is, 12 and 8, respectively. The atoms in FCC cells appear to be denser, as indicated by both the coordination numbers and APF [65].

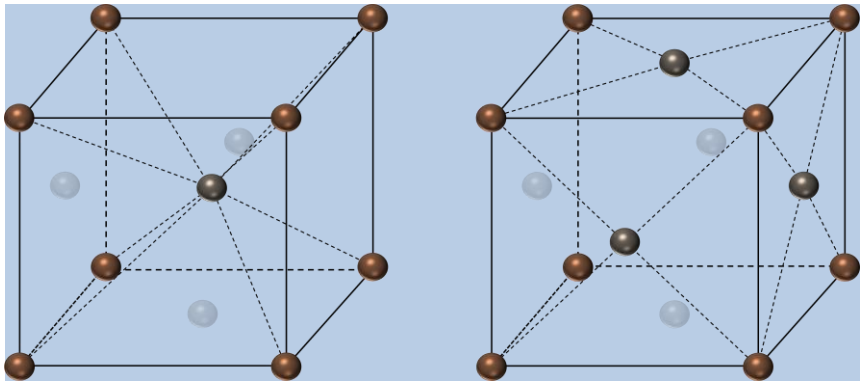

Figure 4: Crystal structure of Ferrite (BCC) and Austenite (FCC) [66].

Chapter 3

Methodology

3.1 Powder

The SAF 2507 (European grade EN 1.4410) powder, which is generated by the process of gas atomization, is provided by Sandvik Osprey, located in Neath, UK. Table 2 displays the chemical composition of the powder. The morphology of the powder particles has a substantial impact on the fluidity and melting characteristics of the powder in the LPBF process. Factors such as the shape and size distribution of the powder particles directly affect the quality of the manufactured samples [6].

Table 2: The chemical composition of SAF 2507 powder.

Element	Content(wt.%)
Fe	Balance
Cr	24.6-25.4
Ni	6.8-7.2
Mo	3.76-4.24
Mn	0.7-1.1
N	0.26-0.31
Si	0.2-0.6
O	0 .08
Cu	0.02
C	0.02
Co	0.02
Al	0.015
P	0.010
Sn	0.010
Ti	0.010
W	0.007
S	0.007
B	0.001

3.2. Design of Experiments

A Design of Experiments (DOE) was created to assess the impact of the SLM process parameters and the laser energy density on the quality of the as-built components. Equation 1 defines the volumetric energy density.

Regression analysis was used to examine the impact of laser power, scan speed, hatch spacing, and energy density on the parameters of the as-built item. A comprehensive factorial design of experiments (DOE) was created, utilizing the response surface methodology to explore a broad spectrum of factors in the selective laser melting (SLM) process. Figure 6 displays a concise flow diagram overview of the process.

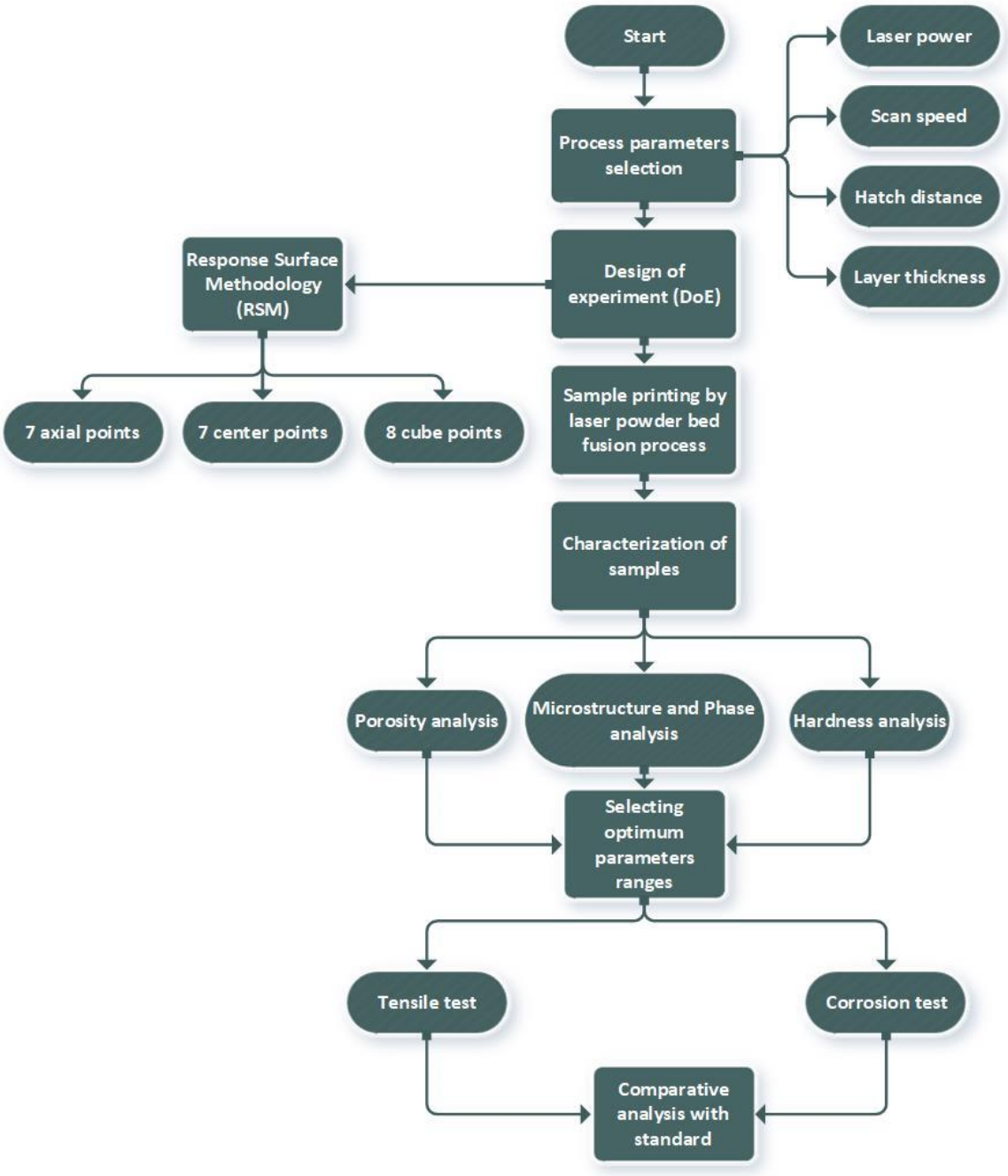

Figure 5. Flow diagram of methodology

3.3.1. Central composite Design (CCD)

The Central composite Design (CCD) is a statistical technique that uses a Design of Experiment (DoE) to produce metrology. It involves fitting a regression model that relates input and output parameters, and subsequently optimizing the process results. The acronym "DoE" stands for Design of Experiments, which encompasses many techniques such as complete factorial, central composite, and box-Behnken. These methods are used to create a series of trials where the results are influenced by the input components. This study focuses on optimizing three factors: laser power (p), scan speed (v), and hatch distance (h). The layer thickness (t) remains constant at 50 µm. The optimization procedure often neglects the layer thickness (t) and maintains it at a constant value. However, it has been discovered that smaller layer thicknesses lead to improved quality [38]. Therefore, a layer thickness of 50 µm was chosen.

The chosen design of experiments (DoE) dictates the quantity of trials, combinations, replication, and randomization of the elements to examine the cause-and-effect connections between inputs and outputs with a specific level of certainty. The number of trials required for a complete factorial Design of Experiments (DoE) with three components, each having five levels, is $5^3 = 125$. Nevertheless, doing 125 experiments (i.e., making and measuring cubes) is not feasible due to the constraints of cost and time. The CCD, or Central Composite Design, is a comprehensive five-level fractional factorial Design of Experiments that includes centre and cube points. It is commonly employed to accurately fit quadratic models. A three-factor central composite design (CCD) consists of 8 cube points, 7 centre points, and 6 axial points. The factorial points (1, -1) for all three components are determined by referencing the prior investigations conducted on SDSS [32-34]. Subsequently, the centre and star points are computed and documented, as seen in Table 3. The star points determine the lowest and highest values for all three criteria. The Central composite design was employed to construct the different run sets shown in Table 3 using Minitab software (version 20, Minitab, Pennsylvania, USA). A set of 21 cylinders, measuring 5 × 10 mm each, were created. Each cylinder was allocated distinct printing parameters settings in accordance with the sequence presented in Table 3.

Table 3. Illustration of a three-factor central composite design (CCD)

	Power	Scan speed	Hatch distance
Axial point	**0**	**0**	**-1**
	-1	**0**	**0**
	0	**1**	**0**
	1	**0**	**0**
	0	**0**	**1**
	0	**-1**	**0**
Centre point	**0**	**0**	**0**
	0	**0**	**0**
	0	**0**	**0**
	0	**0**	**0**
	0	**0**	**0**
	0	**0**	**0**
	0	**0**	**0**
Cube point	**-α**	**-α**	**α**
	α	**-α**	**-α**
	-α	**α**	**α**
	-α	**α**	**-α**

	-α	-α	-α
	α	-α	α
	α	α	-α
	α	α	α

3.2. LPBF Processing Strategy

The three essential parameters, laser power, scan speed, and hatch distance/spacing, were methodically altered based on the CCD model, considering normalization through energy density (Eq. 1) as presented in Table 3. It is important to note that the layer thickness remained constant at 50 µm. The parameter range is determined after an in-depth review of relevant literature [67-69], have a laser power, scan speed, and hatch spacing of (100-300) W, (250-1000) mm/sec, and (50-180) µm, respectively. The study investigated a range of energy densities, ranging from 21.4 J/mm^3 to 168.9 J/mm^3, by adjusting the three LPBF parameters individually, as shown in Table 5. The levels and corresponding values of the CCD factor are shown in Table 4. Cylindrical samples were constructed for each parameter set, with dimensions of 10 mm in length and 5 mm in diameter.

Table 4. CCD factor levels and values.

Levels	Laser Power (W)	Scan Speed (mm/s)	Hatch Distance (µm)	Layer Thickness(µm)
Lowest (−1)	100	250	50	50
Lower (− α)	140	402	76.4	50
Centre point (0)	200	625	115	50
Higher (α)	259.5	848	154	50
Highest (1)	300	1000	180	50
Range	100–300	250–1000	50–180	50

Table 5. Various parameters set based on central composite design.

Sample NO.	Power(W)	Scan speed(mm/s)	Hatch distance(µm)
1	200	625	115
2	200	625	115
3	100	625	115
4	200	625	50
5	200	625	180
6	140	402	76.4
7	200	625	115
8	259.5	402	154
9	200	625	115

10	200	625	115
11	259.5	848	154
12	200	250	115
13	140	848	76.4
14	140	402	154
15	140	848	154
16	200	1000	115
17	200	625	115
18	300	625	115
19	259.5	402	76.4
20	259.5	848	76.4
21	200	625	115

As shown in Table 5, twenty-one samples with distinct parameter configurations were manufactured. From a total of 21 samples, a subset of 15 samples has been selected as the representative sample for further analysis in this research. Hence, the updated parameters are displayed in Table 6.

Table 6. Selected parameters set for further investigation.

Sample NO.	Power(W)	Scan speed(mm/s)	Hatch distance(μm)
1	200	625	115
2	100	625	115
3	200	625	50
4	200	625	180
5	140	402	76.4
6	259.5	402	154
7	259.5	848	154
8	200	250	115
9	140	848	76.4
10	140	402	154
11	140	848	154
12	200	1000	115
13	300	625	115
14	259.5	402	76.4
15	259.5	848	76.4

Among the 15 samples, each with different parameter combinations, the seven most suitable parameters set have been selected for manufacturing the tensile test samples. Each parameter set is printed twice, as shown in Table 7.

Table 7. Selected parameters set for Tensile sample.

Sample No.	Power	Scan Speed	Hatch distance
1	200	625	115
2	200	625	115

3	245	625	115
4	245	625	115
5	300	625	115
6	300	625	115
7	200	1000	115
8	200	1000	115
9	200	402	115
10	200	402	115
11	200	625	180
12	200	625	180
13	200	625	76
14	200	625	76

3.3. Manufacturing of Specimen

Figure 6 displays the manufactured samples with 3D design. The SLM SOLUTIONS 280 2.0 machine (fig. 2) from Mechatronics Innovation Lab AS was used to create all the samples. The SLM SOLUTIONS 400W printer utilizes an IPG 150 fibre laser operating at a wavelength of 1070 nm. The laser has a beam width of 60 µm and a maximum power output of 400 W. It can achieve a scanning speed of up to 10 m/s and has a minimum feature size of 150 µm. All samples were printed in an argon atmosphere with a consistent oxygen concentration of 0.01%. Twenty-one cylindrical samples measuring 10x5 mm were produced utilizing 21 distinct datasets (as displayed in Table 5). The stripe scanning approach was used for all samples. The scanning direction between consecutive layers was maintained at 67^0, without any re-melting techniques as seen in figure 7.

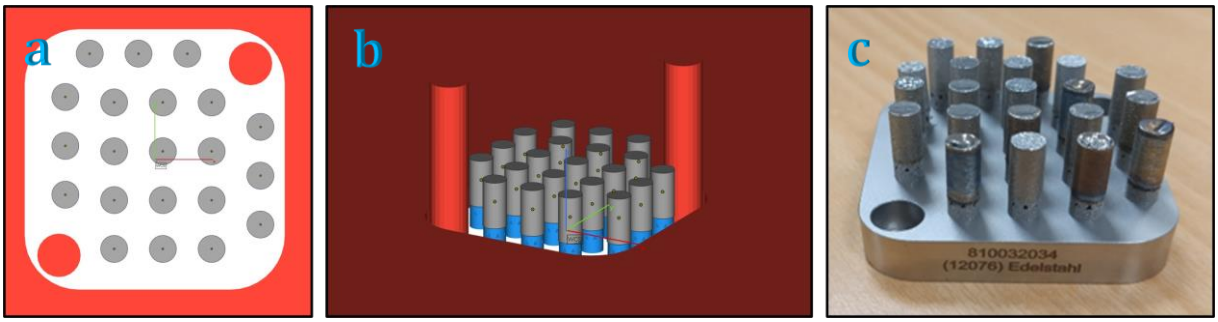

Figure 6. SLM Printed 21 cylindrical Samples with different parameters set. (a) Top view of CAD design, (b) 3D view of CAD design, and (c) Manufactured samples.

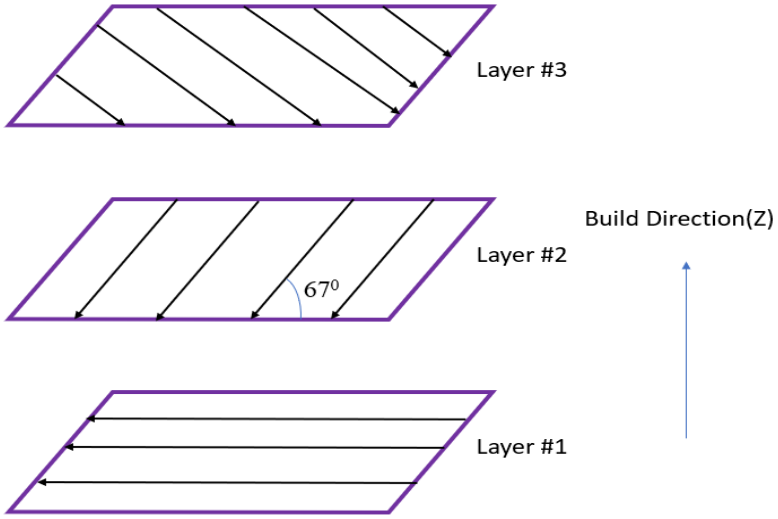

Figure 7. Illustration depicting a stripe scan pattern. Each subsequent layer causes the stripes to rotate at an angle of 67° relative to the preceding layer.

The 3D design of tensile test samples and the as-built samples for tensile testing, according to the parameters specified in Table 7, are depicted in Figure 8.

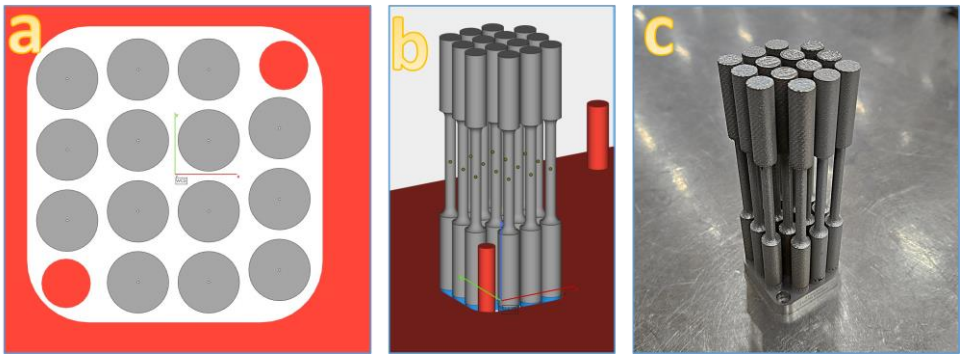

Figure 8. SLM Printed 14 cylindrical Samples with different parameters set. (a) Top view of CAD design, (b) 3D view of CAD design, and (c) Manufactured samples for tensile test.

3.4. Specimen Preparation

3.4.1. Hot Mounting

Following the specimen's cutting, the hot mounting technique depicted in Figure 9 is employed to facilitate the handling of the specimens during metallurgical operations, such as grinding, polishing, LOM analysis, SEM analysis, and hardness analysis.

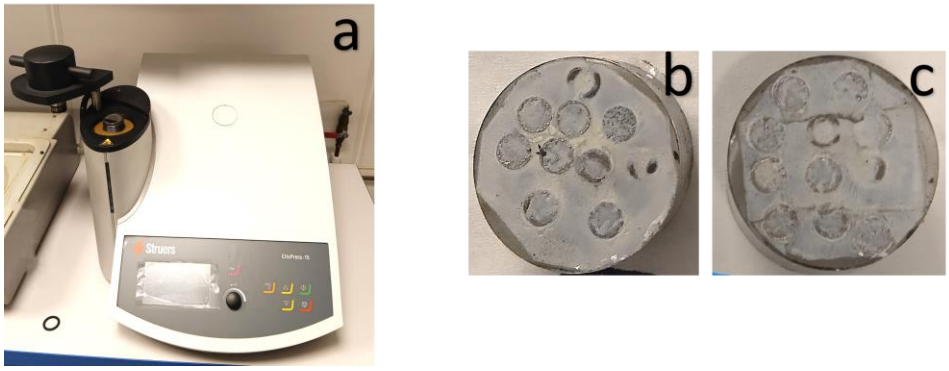

Figure 9. (a) Struers Citopress-15, (b) and (c) Hot mounted sample

The Struers CitoPress-15 device was utilized to fabricate the test discs using condofact, a fast-casting synthetic resin that is electrically conductive and well-suited for electrolytic etching.

3.4.2. Grinding and Polishing

Grinding and polishing are procedures used to achieve a flawless scratch-free, and reflective surface of the specimen for microscopic analysis. The Struers Tegraforce-30 machine was utilized for the specific tasks of grinding and polishing, as seen in Figure 10. The samples were ground using SiC-Paper with grit sizes of P220, P1200, P2400, and P4000. Following that, the specimen underwent polishing with polishing cloths coated with MD-Dac diamond suspension.

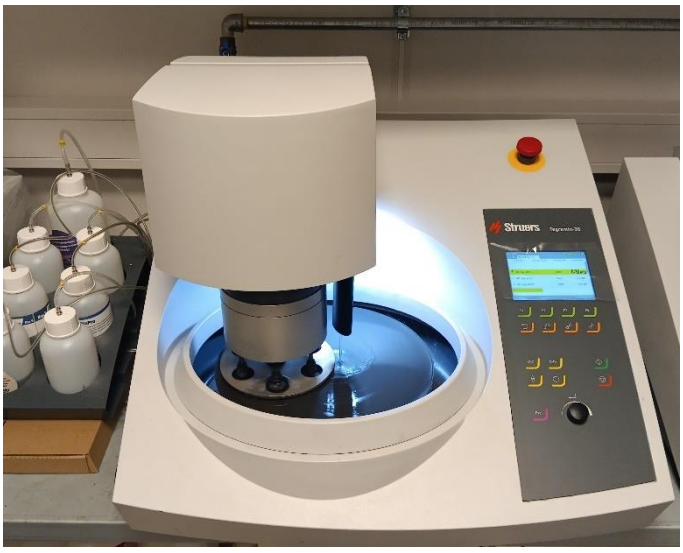

Figure 10. Struers Tegraforce-30 machine.

3.4.3. Electrolytic polishing and Etching

The specimens underwent etching using a 20% NaOH solution at 5V for a duration of 10 seconds, with the purpose of conducting phase analysis. Following the etching process, the material underwent water washing, ethanol cleaning, and air drying.

3.4.4. Experimental setup for Optical Microscope

Following the grinding, polishing, and etching procedures, the material was analysed using the Zeiss Axio Imager.A1m light microscope, as shown in Figure 11, to obtain a comprehensive understanding of the microstructure and distribution of phases in the sample. The materials were examined at magnifications ranging from 2.5 to 50 times.

Figure 11. Optical Microscope Zeiss Axio Imager.A1m

3.4.5. Experimental setup for Hardness measurement

The hardness test is a reliable method for assessing a material's ability to withstand plastic deformation. The specimens were meticulously polished to achieve a sleek surface to quantify the indentation mark accurately. The grinding and polishing methods for the optical microscope sample were identical. The hardness tests were conducted using the Zwick Roell DuraScan 50 test machine (Figure 12) with a load of 10 kg, specifically HV10, and a dwell duration of 10 seconds. Every sample was assessed at 3 to 5 distinct locations of indentation.

Figure 12. Zwick Roell DuraScan 50 hardness test machine.

3.5. Microstructure Analysis

Light optical microscopy (LOM) was used to analyse the microstructure of as-built samples of SAF 2507. The Zeiss Axio Imager.A1m microscope was utilized to assess the microstructure of the etched components. The polishing and etching operations were conducted in accordance with the guidelines provided by Maamoun et al. [2].

3.6. Mechanical Testing

The microhardness measurement was conducted in accordance with the ASTM E384-17 standard using a Zwick Roell DuraScan 50 testing apparatus. The mean microhardness values of the samples were determined on the XY-plane, which is parallel to the deposited layers. The recorded values were obtained by averaging 5-10 indentations made on the tested surface with a 10 Kg weight applied for a duration of 10 seconds. The findings were then analysed using ecos Workflow Pro software. The tensile rod samples were created and manufactured in accordance with the specified geometry and dimensions given in ISO 6892-1. The tensile test was conducted following the ISO 6892-1standard protocols utilizing a SI-Plan Universal load system with a maximum load capacity of 25 kN.

3.7. Ferric Chloride Pitting Test

The ASTM G48 Test is a set of standardized methods used to evaluate the resistance of stainless steels and related alloys against pitting and crevice corrosion. This is done by subjecting the materials to a ferric chloride solution. The experiment utilizes method A, specifically the Ferric Chloride pitting test [70].

3.7.1 Sample Preparation

The sample underwent grinding and polishing using SiC paper with grit sizes of P220, P800, P1200, and P2400, as seen in Figure 13. Due to its cylindrical shape, uniform polishing was a tough task. The sample's sharp edges were further smoothed by the process of grinding and polishing. The sample's dimension was assessed, and the overall exposed area was computed. Subsequently, the specimen underwent thorough rinsing with water, immersion in acetone, and subsequent drying by exposure to air. The sample was measured with precision to the closest 0.0001g.

Figure 13. Surface polishing of corrosion test sample.

3.7.2. Preparation of Ferric Chloride Test Solution

Dissolve 100 grams of ferric chloride, $FeCl_3 \cdot 6H_2O$, in 900 millilitres of Type IV reagent water, resulting in a solution with approximately 6% $FeCl_3$ by mass. Pass the mixture through glass wool or filter paper to eliminate insoluble particles [70].

3.7.3. Apparatus Required

- Beaker
- Supporting Specimen
- Nylon Wire
- Thermometer
- Plastic lid

3.7.4. Procedure

A solution was prepared by dissolving 100 g of Reagent grade ferric chloride $FeCl_3.6H_2O$ in 900 ml of distilled water, resulting in a solution with a concentration of 6% $FeCl_3$ by mass. The solution volume for the tested specimen was guaranteed to be a minimum of 5 ml per square centimetre of surface area. Due to the conduction of the corrosion test at ambient temperature, the use of a water bath was unnecessary. The solution was transferred into the beaker, and samples were secured with slender nylon wire and suspended on plastic rods. Once the solution had achieved the target temperature of 22 ± 2˚C, the samples were submerged in the solution [70]. Following the immersion of the specimens in ferric chloride solution contained in beakers, plastic covers were employed to shield the beakers and prevent the test solution from evaporating. It remained

at that location for a duration of 24 hours. Following the immersion of the specimens in ferric chloride solution within beakers, plastic covers were employed to shield the beakers and inhibit the evaporation of the test solution. Upon finishing the test, the specimens underwent a water washing, followed by the utilization of a nylon brush to eliminate corrosion products. Following the cleaning process, the items were immersed in acetone for a duration of 15 minutes and subsequently allowed to air dry at ambient temperature for a period of 24 hours. The dried specimens were initially examined for the presence of pits, followed by the measurement of their weight loss. Ultimately, a microscope was employed to conduct a more thorough analysis of the surface of the material [70]. The corrosion rate can be determined by utilizing the formula presented below.

$$\text{Corrosion rate} = \frac{Wt_i - Wt_f}{A} \qquad \text{.....equation 2}$$

Wt_i and Wt_f represent the weights of the sample before and after the test, respectively, whereas A denotes the exposed surface area.

Chapter 4

Results and Discussion

The investigation in this chapter started by examining the morphology of SAF 2507 powder. Porosity, microstructure, tensile strength, and elongation are analysed in this chapter in relation to the influence of LPBF process parameters including laser power, scan speed, and hatch spacing as well as the resulting laser energy density. In the concluding section of the chapter, the corrosion rate is studied with particular emphasis on the sample characterized by the lowest porosity.

4.1 Powder Characteristics

SAF 2507 powder's morphology was characterized using SEM and the images are shown in Figure 14(a, b). It can be seen in SEM images, most of the particles have spherical shape morphology with a small number of satellites. Further, the particle size distribution (PSD) was measured using image J software from the SEM image, and the result is shown in Figure 14c. As shown in Figure 14(c), the PSD of the powder varies from 19 to 55 µm. The typical powder size, represented by D10, D50, and D90, was 22, 32.3, and 44.8 µm, respectively.

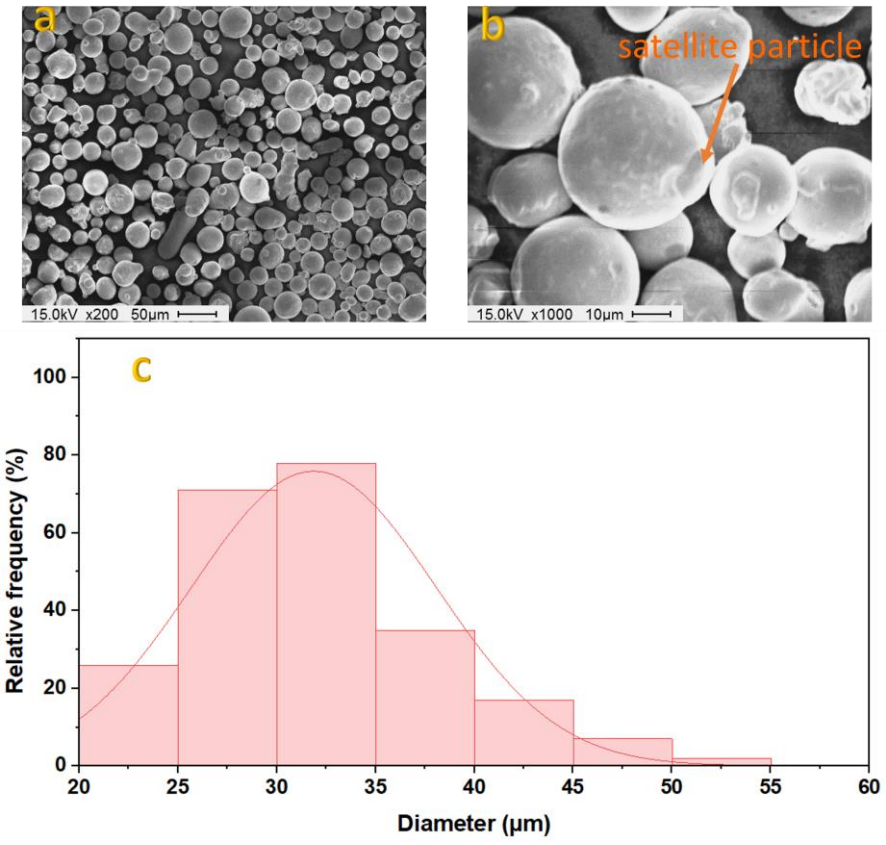

Figure 14. (a) Scanning electrode micrograph of the gas atomized SAF 2507 powder, (b) SAF 2507 powder with satellites, and (c) size distribution of the SAF 2507 alloy powders.

4.2. Porosity Characterization analysis of SLM printed parts.

Porosity is a prominent flaw that occurs during LPBF metal additive manufacturing. Porosity is a crucial property that directly or indirectly affects the mechanical and microstructural properties of manufactured parts [71]. The most critical aspect to be considered in AM is the densification of the material. To get a more compact product, it is necessary to have an optimum set of process parameters. This section focuses on the pore's formation and the influence of process parameters on porosity. The porosity of all samples listed in Table 6 was measured and documented in Table 8.

Table 8. The SLM process parameters applied for fabricating the SAF 2507 samples.

Sample No.	Power(W)	Scan Speed(mm/s)	Hatch Distance (µm)	Layer Thickness(µm)	Laser Energy Density(j/mm^3)	Porosity (%)
1	200	625	115	50	55.7	0.02
2	100	625	115	50	27.8	9.03
3	200	625	50	50	128	0.42
4	200	625	180	50	35.6	0.73
5	140	402	76.4	50	91.2	1.18
6	259.5	402	154	50	83.8	0.58
7	259.5	848	154	50	39.7	0.28
8	200	250	115	50	139.1	3.68
9	140	848	76.4	50	43.2	0.04
10	140	402	154	50	45.2	0.76
11	140	848	154	50	21.4	12.86
12	200	1000	115	50	34.8	0.22
13	300	625	115	50	83.5	0.06
14	259.5	402	76.4	50	169	3.97
15	259.5	848	76.4	50	80.1	0.06

4.2.1. The Effect of laser Power on the Porosity

An investigation was conducted to analyse the impact of laser power on the porosity of LPBF of SAF 2507. Three different laser powers of 100, 200, and 300 W were utilized, with the scan speed, hatch spacing, and layer thickness maintained at 625 mm/sec, 115 µm, and 50 µm, respectively. This is shown in Table 6 as an experiment set. The dark contrast colour indicates the presence of pores in the SAF 2507 samples throughout this study. As illustrated in Figure 15a, the maximum porosity (%) was obtained by employing a laser power of 100 W. The as-built sample produced by a 100 W laser exhibiting irregularly shaped porosity. This irregularity is attributed to lack of fusion (LOF) and residuals in interparticle gaps. At lower laser power levels, it is seen that the melt pool and, consequently, the scan track will be narrower and shallower. This results in insufficient fusion between neighbouring tracks and between successive layers [72].

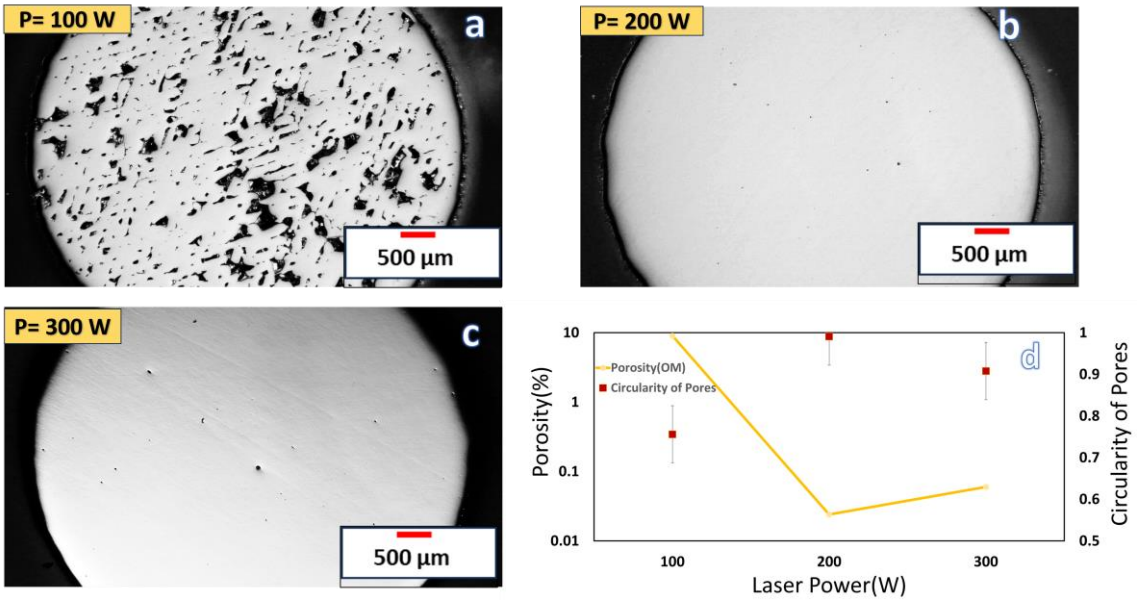

Figure 15. Optical micrographs as a function of different the laser power of (a)100 W, (b) 200 W, and (c) 300 W with the scan speed, and hatch spacing held constant at 625 mm/s, and 115 µm, respectively. (d) Percentage of porosity distribution (logarithmic) and Circularity of pores with different laser power(W).

The porosity decreased as the laser power increased from 100 W. The observation is evident in Figure 15b, where an increase in power (as seen in Figure 15d) leads to porosity decrease, followed by a progressive rise in randomly distributed pores with rounded forms. In the intermediate region, when porosity is limited, only little spherical pores are present. These metallurgical pores result from trapped gas between the particles. The further increase of laser power to 300 W, above the laser power of 200 W, resulted in a notable increase in the presence of spherical pores, as seen in Figure 15c. The presence of these roundish pores can be defined as keyhole porosity. This occurs when excessive laser power creates a deep melt pool with rapid dynamics, resulting in the trapping of vapours within the pores as the melting pool advances and the vapor cavity collapses. These are most likely the gas-filled pores that develop during the process of solidification. It is worth noting that at a constant scanning speed, there are distinct thresholds below which lack of fusion pores becomes the dominating issue. However, the formation of keyhole pores only occurs when the vapor depression becomes unstable at higher laser power [26]. Thus, while the scan speed, hatch spacing, and slice thickness were constant, the power variation resulted in different porosity formation. At lower power, insufficient fusion occurred, whereas higher laser power led to increased keyhole porosity.

4.2.2. The Effect of Scan Speed on the Porosity

Figure 16 presents LOM images and porosity percentage of cylindrical samples built with varying scan speed, from 250 to 1000 mm/sec, while the laser power, hatch spacing, and layer thickness were held constant at 200 W, 115 µm, and 50 µm, respectively. This is listed as an experiment in Table 8. The variation of scan speed on porosity is less significant than the variation of laser power but more significant than the variation of hatch spacing. The lowest porosity was observed when a scan speed of 625 mm/s was used. Figure 16(a) illustrates the presence of larger pores in the sample produced with lowest scan speed of 250 mm/s. As the scanning speed lowers, the time

required for laser action per unit length of scanning is higher. Consequently, the powder's heat absorption rises, leading to a progressive increase in the amount of melted powder per unit length. The melting pool's width and height gradually expands. Thus, the pool that was previously melted undergoes remelting, leading to the creation of keyhole porosity [73].

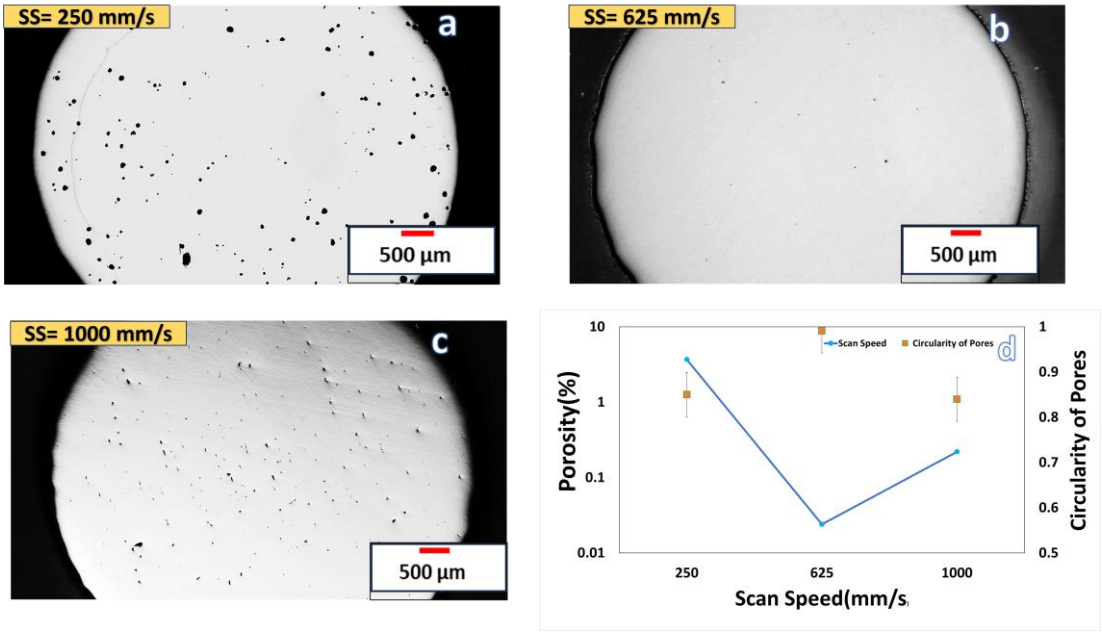

Figure 16. Optical micrographs as a function of different Scan Speed of (a) 250 mm/s, (b) 625 mm/s, and (c) 1000 mm/s with the Laser power, and hatch distance held constant at 200 W, and 115 µm, respectively. (d) Percentage of porosity distribution (logarithmic) and Circularity of pores with different Scan Speed (mm/s).

If the scan speed increases from 250 mm/s, remelting decreases resulting in lower keyhole porosity. At the scan speed of 625 mm/s the generates lower porosity called metallurgical pore because of gas entrapped in melting zone. A further increase in scan speed resulting in lack of fusion pore, corresponding to a scan speed 1000 mm/s because of lowering exposure time given to a specific length, as shown in figure 16c. Thus, particles don't get enough heat to melt, resulting in irregular shape pores. There exist some unmelted particles in between lack of fusion pore. Figure 16(d) reveals that the keyhole porosity is more prevalent than the lack of fusion porosity.

4.2.3. The Effect of Hatch Spacing on the Porosity

Figure 17 presents percentage of porosity determined from cylindrical samples produced by varying the hatch spacing from 50 to 180 µm, while the laser power, scan speed, and layer thickness were held constant at 200 W, 625 mm/sec, and 50 µm, respectively. This is listed as an experiment in Table 8. From figure 4(d), it is seen that the variation of hatch distance is not significant as Laser power. As seen in Figure 17(b) the lowest porosity was observed when a hatch spacing of 115 µm was used; the porosity increased when the hatch spacing was lower or higher than 115 µm. Notably, at a lower hatch spacing of 50 µm, as depicted in Figure 17a, keyhole porosity becomes more prominent because of overlapping between hatches. As the hatch distance increases from 50 µm in Figure 17b, remelting diminishes, resulting in lower keyhole porosity. Specifically, at a hatch distance of 115 µm, lowest porosity is observed, referred to as metallurgical

pore, attributed to gas entrapped in the melting zone as seen in Figure 17b. Further increasing the hatch distance from 115 µm, the width of the new track did not completely cover the spacing between the hatches, leading to insufficient fusion between the tracks. Figure 17c illustrates the presence of larger pores in the sample produced with the maximum hatch spacing of 180 µm. When the space between hatches is increased, the heat received by neighbouring tracks is insufficient to melt the material due to less overlap between molten spots and adjacent tracks. This leads to the formation of irregularly shaped pores [74]. Additionally, there exist some unmelted particles interspersed within lack of fusion pores.

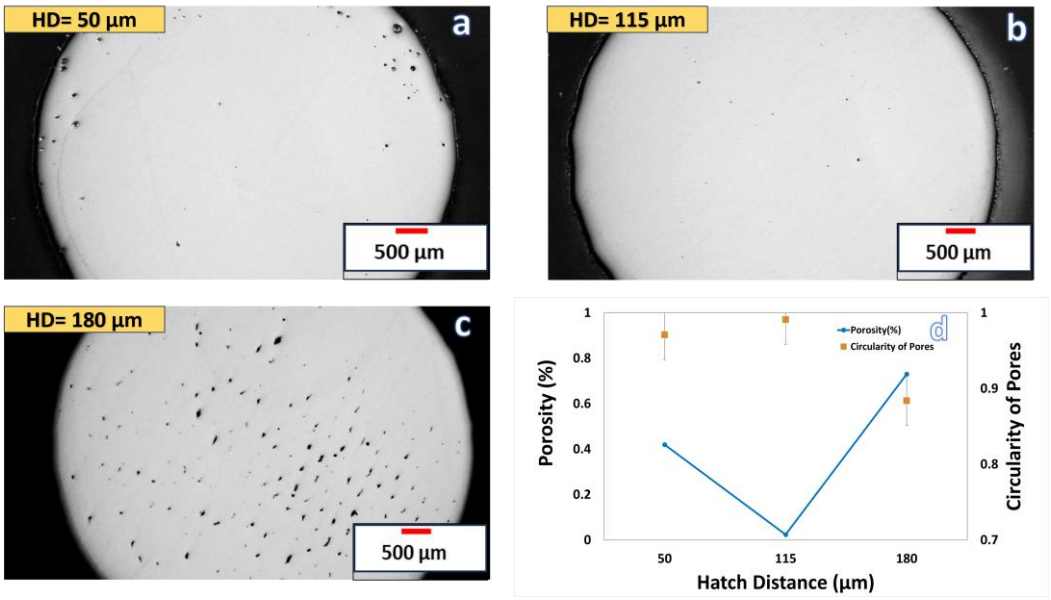

Figure 17. Optical micrographs as a function of different hatch distance of (a) 50 µm, (b) 115 µm, and (c) 180 µm with the Laser power, and Scan Speed held constant at 200 W, and 625 mm/s, respectively. (d) Percentage of porosity distribution (logarithmic) and Circularity of pores with different hatch distance (µm).

Nevertheless, the degree of variation in porosity with hatch spacing decreased to some extent when the optimum laser power, scan speed, and slice thickness were used at 200 W, 625 mm/sec, and 50 µm, respectively.

4.2.4. Influences of overall laser energy density on porosity

Figure 18 shows light optical microscopic (LOM) images obtained in the printing direction (XY-plane) of SAF 2507 samples produced with various laser energy density investigated in Table 8. Figure 18 also shows that the energy density values ranging from 43.4 to 83.8 J/mm^3 resulted in materials with a porosity of less than 1%. The literature reports an optimal energy density range of 38 to 63 J/mm^3 with the porosity remaining below 3% while the laser energy density varied [75].

Lower laser energy density, for example, resulting from either high laser scan speed, larger hatch spacing, or lower laser power at a constant layer thickness, yielded more irregular-shaped flaws

due to insufficient melting, i.e., lack of fusion flaws [76]. Figure 18a illustrates that process-induced porosity or lack of fusion pores of 250–300 µm size and irregular shapes are formed at a low energy density of 21.5 J/mm^3. The part produced with a lower energy density may have unmelted particles because of insufficient powder melting to the melted layer, which results in a porous structure. As the laser energy density increases, the probability of lack of fusion porosity decreases, and the particles receive sufficient energy for adequate melting. Figure 18(a-h) displays light optical micrographs of the SAF 2507 sample, fabricated using an energy density range of 21.5 to 55.6 J/mm^3. The minimum amount of porosity, in terms of both quantity and size, is attributed to the sufficient energy density of 55.6 J/mm^3 as seen in Figure 18h. As the figure 18h sample produced at higher energy density than figure 18a, the lack of fusion pores almost disappeared but there exist gas pores. These flaws and/or pores appear within the intermediate volumetric energy density range of 43.4 to 83.8 J/mm^3. A further increase in laser energy density led to the formation of more spherical pores, which can be attributed to the keyhole effect. The higher energy density creates a steep "V" shaped melt pool, which leads to micro evaporation from the melt pool; that gas is trapped below the melt pool, which again results in porosity [77]. As a result of the higher energy density, Figure 15o sample exhibits a larger keyhole porosity in comparison to figure 15h sample.

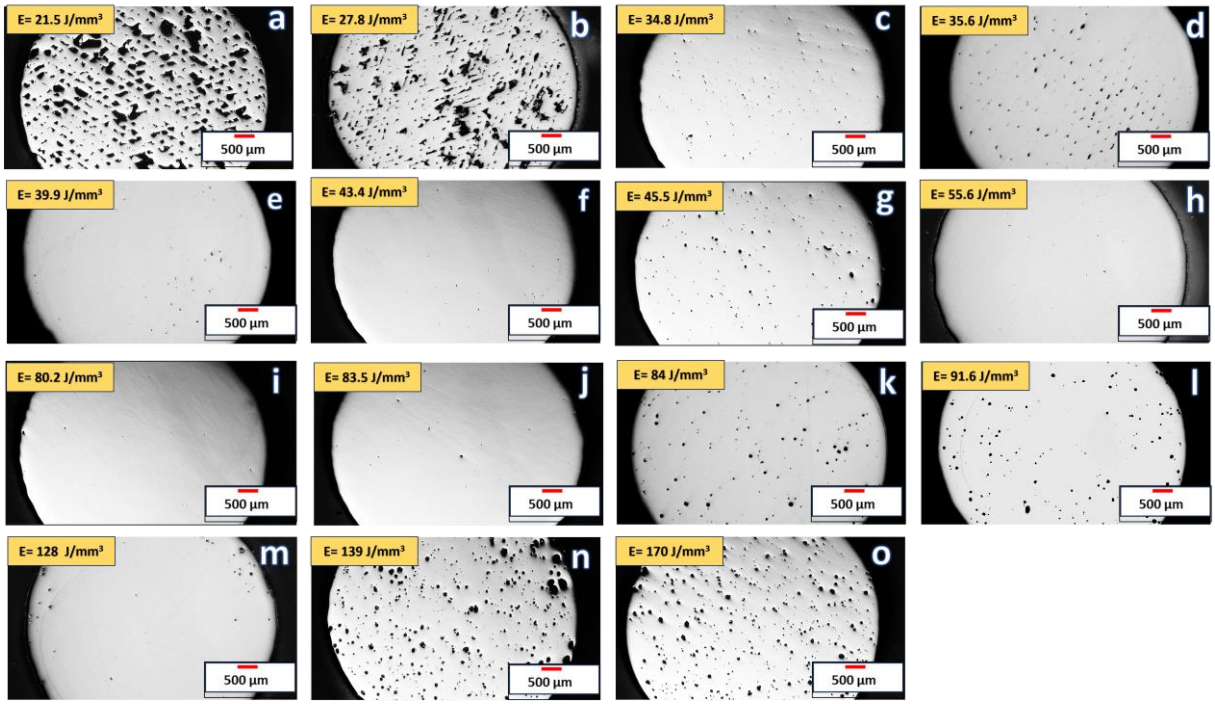

Figure 18. Optical micrographs from the cross-sections perpendicular to the build direction for LPBF SAF 2507 built as functions of different laser energy density.

It is important to mention that the laser energy density level has a substantial impact on the rate at which solidification occurs. As a result, particular porosity features are formed based on the values used [3].

Moreover, Figure 19a presents the percentage and types of porosity determined from samples produced by LPBF as function of various laser energy employed as listed in Table 8. In Figure 19a, porosity (%) decreased sharply with an increase in laser energy density, remained up to 0.024% at energy density 55.6 J/mm^3, then increased gradually with a further increase in laser energy density. Porosity lower than 1% was observed for the sample produced with the laser energy

density from 43.4 to 83.8 J/mm^3 as shown in Figure 19a. The minimum porosity of 0.024% was observed for the sample of energy density of 55.6 J/mm^3.

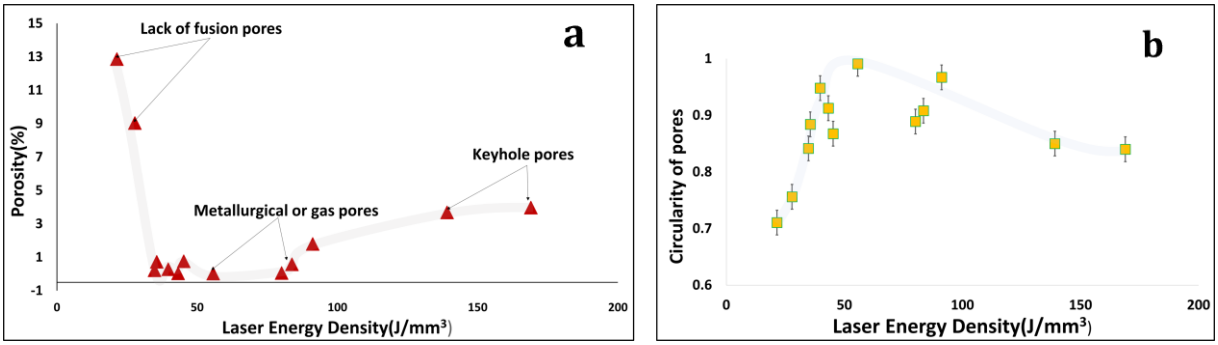

Figure 19. (a) Percentage of porosity distribution, and (b) Circularity of pores with Laser energy density (J/mm^3).

The correlation between the circularity of pores, which varies from 0.71 to 0.97, and the laser energy density, which ranges from 21.4 to 169 J/mm^3, is depicted in Figure 19b. A significant decrease in circularity below 1 would indicate lack-of-fusion pores, whereas circular pores approaching 1 would be more likely to represent metallurgical or keyhole pores. Pores with much reduced circularity were found at low energy density, where the development of lack-of-fusion pores resulting from inadequate melting occurs. Pores with a circularity value approaching 1 in laser energy density of 55.6 J/mm^3 are more likely to represent metallurgical or gas-trapped pores. At very high energy density pores with somewhat reduced circularity have been found, where keyhole pores occur. This is attributed to the fusion of several keyhole pores. From Figure 19b it is observed that energy density ranged from 43.4 to 80.1 J/mm^3, which was associated with a porosity level below 1% and circularity over 0.90. Hence, this is the optimal LPBF parameter range established in this investigation. The crucial parameter for achieving a dense product is the optimum laser energy density, which may be attained by carefully selecting the laser power, scanning speed, hatch spacing, and layer thickness.

In Figure 20a, b, there is an observed correlation between the increase in laser power and the variations in speed and hatch patterns depicted in the plots of (laser power*scan speed) and (laser power*hatch spacing). Moreover, the Figure 20c (scan speed*hatch spacing) plot clearly demonstrates that raising the speed has a noticeable impact on the different hatch curves, suggesting a significant interaction effect among the three parameters.

Figure 20a displays the quantitative porosity data, illustrating the laser power variation for three distinct scan speeds: 402 mm/s, 625 mm/s, and 884 mm/s. The results demonstrate that the optimum laser power range for achieving minimal porosity decreases as the scan speed decreases. It is apparent that a lower scanning rate necessitates less laser power to generate a melt pool of equivalent size. Furthermore, it has been observed that lower laser power combined with faster scan speed leads to increased porosity, whereas higher laser power combined with slower scan speed results in increased porosity. At a consistent laser power, a higher scan speed results in an increased presence of a lack of fusion porosity, whereas a lower scan speed leads to a higher presence of keyhole porosity (as depicted in Figure 16d). These results also demonstrate that for a fixed scan speed, the keyhole porosity grows in both extent and size as the power increases. This can be attributed to the larger vapor cavity formed at higher power levels. Higher

laser power together with faster scanning speed results in a wider range and reduced occurrence of keyhole mode porosity. The higher scanning velocity also reduces instability in the vapor cavity, which aligns with the previous research [77].

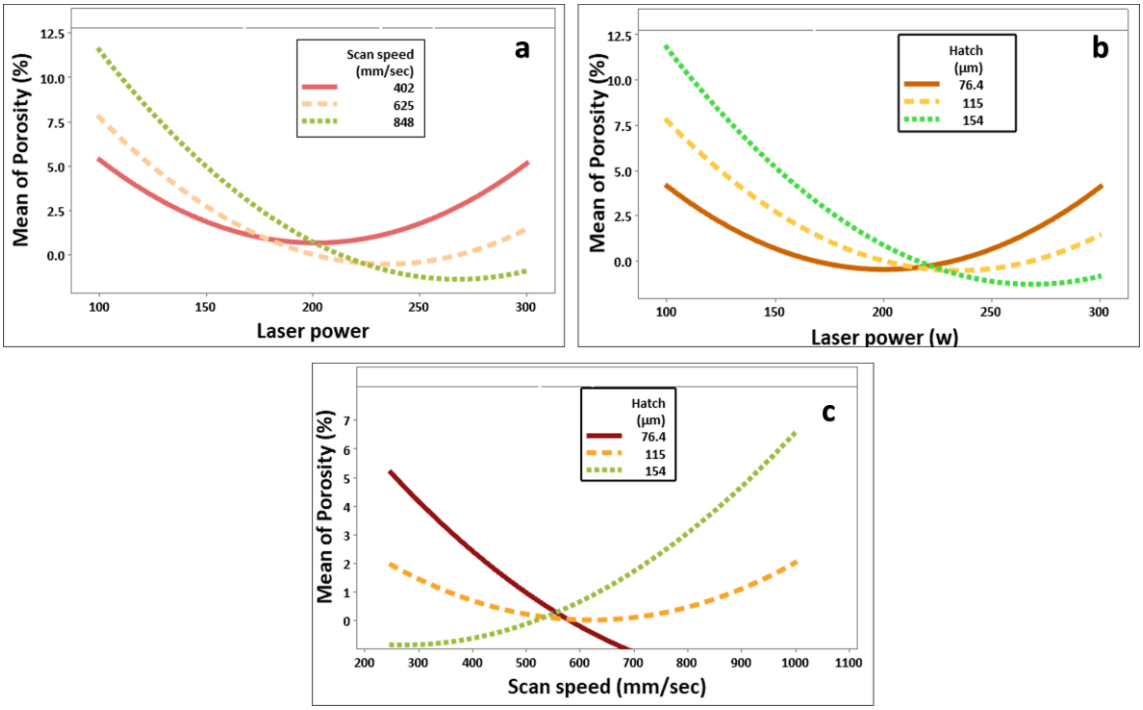

Figure 20. Factor vs. Interaction plots for porosity (%), (a) Laser power* Scan speed, (b) Laser power* Hatch speed, and (c) Scan speed * Hatch speed.

The porosity (%) is depicted in Figure 20b, demonstrating the variation in laser power for three different hatch spacings: 76.4, 115, and 154 µm. It is observed that at lower laser power, less overlap, and remelting occurs as hatch spacing rises, leading to a lack of fusion between neighbouring tracks. Similarly, figure 20c shows that reduced porosity is the result of lower hatch spacing combined with faster scan speed, while reduced porosity is the result of higher hatch spacing combined with slower scan speed.

The influence of laser power, scan speed, and hatch spacing on the sample porosity was demonstrated using three-dimensional (3D) surface graphs and the corresponding contour plots shown in Figure 21. Figure 21a, b illustrates the impact of laser power along with scan speed on porosity at a fixed hatch distance of 115 µm. Higher porosities are observed when there is a combination of either decreased laser power and increased scan speed, or increased laser power and decreased scan speed.

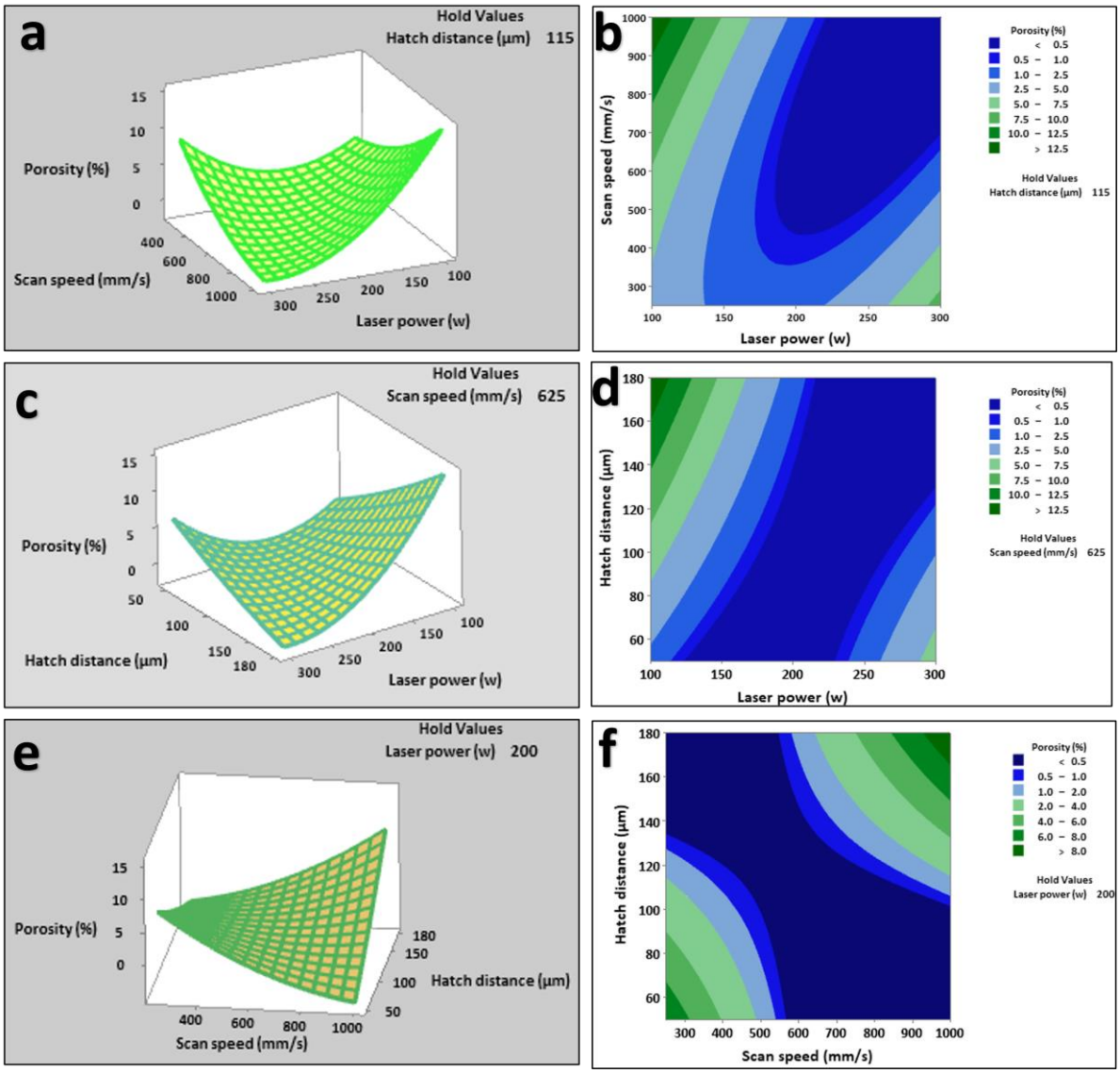

Figure 21. Laser power, scan speed, and hatch distance influence on the porosity: (a, c, e) surface plots; (b, d, f) counter plots

The effects of hatch distance and laser power on porosity are displayed in Figures 21c, d at a fixed scan speed of 625 mm/s. It seems that when there is a combination of either increased laser power and decreased hatch spacing, or decreased laser power and increased hatch spacing, larger porosities are observed.

At a fixed laser power of 200 W, Figure 21e, f illustrates how the hatch distance and scan speed affect the resultant porosity. High porosity levels are produced by either lesser scan speeds combined with lower hatch distances or higher scan speeds combined with larger hatch distances.

4.3. Process parameters influence on Microstructure.

The practical application of LPBF in recent years has proved the effectiveness of SAF 2507. SDSS is well known for its two phases microstructure with nearly equal composition of approximately 50% ferrite & 50% austenite. The LPBF procedure results in the formation of a mostly ferritic microstructure due to its rapid cooling rates at high laser energy density.

In Figure 22, the microstructure of SAF 2507 is shown, where the white/bright phase is austenite, and the grey/black phase is ferrite. The initial ferrite formation is followed by austenite nucleation and growth at ferrite–ferrite grain boundaries [40]. Figure 22a shows that the melt pool solidified with an elliptically shaped profile, and that these melt pool shapes overlap in a specific arrangement according to the value of hatch spacing used. This shape is related to the Gaussian distribution of laser beam power [2]. In comparison to the sample produced at an energy density of 21.4 J/mm^3 in Figure 22a, the melt pool shape geometry in Figure 22g is larger due to getting sufficient heat to melt as the energy density increases to 55.6 J/mm^3. A coarser grain structure is also present inside and along the borders of the melt pool shape as illustrated in Figure 22g. The melt pool shape geometry of the Figure 22l sample is further enlarged compared to the figure 22g sample due to a higher solidification rate together with an energy density increase. The grain structure is coarser than figure 22g sample.

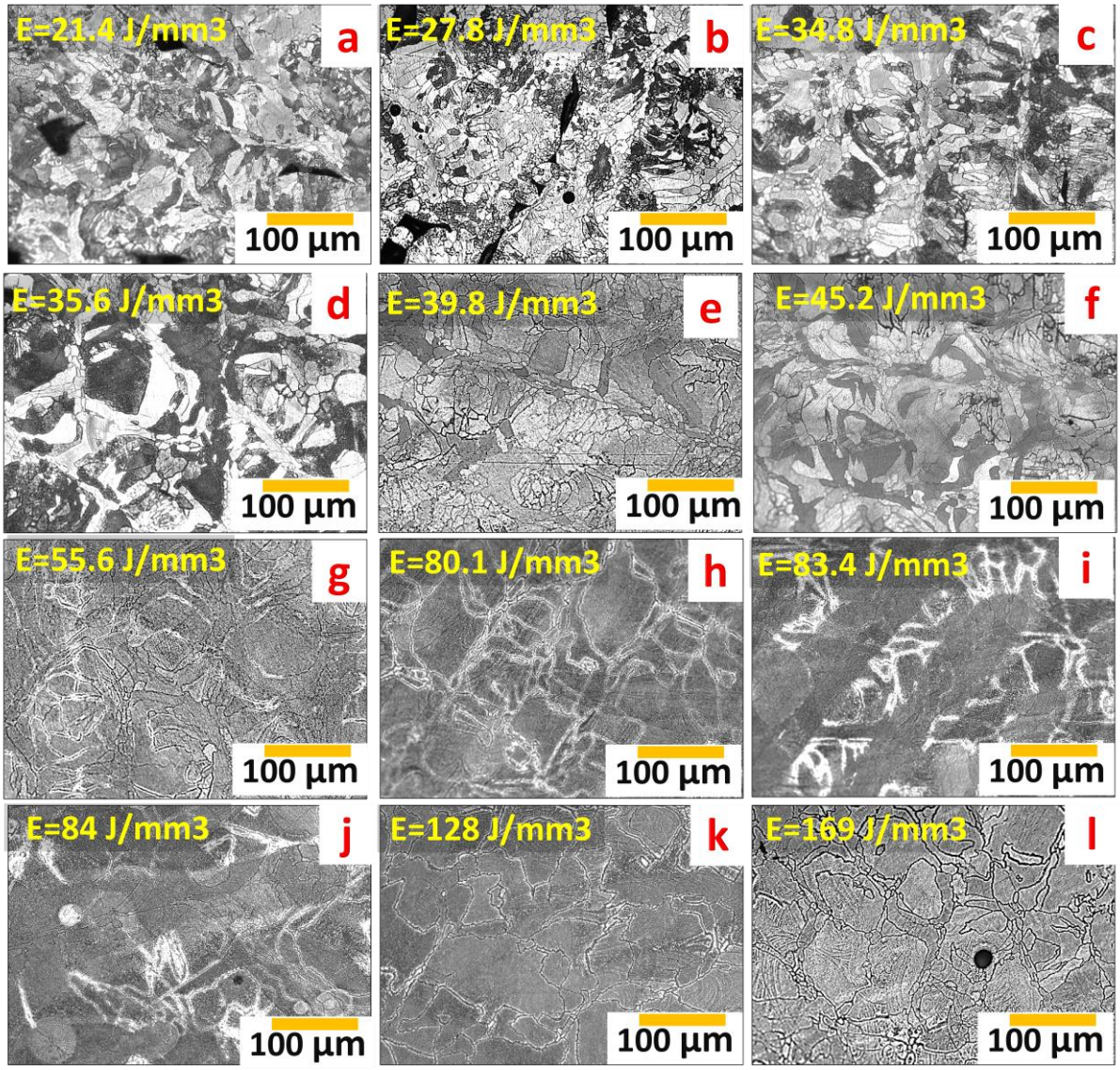

Figure 22. Microstructure (light optical microscope) of the as-built SAF 2507 samples processed under different laser energy density.

At lower energy density, the austenite phase grows roughly equal portion of ferrite phase. Ferrite phase dominates as an increasing laser energy density from 45.2 J/mm^3. As seen Figure 22(a-d), in lower energy density there is a formation of austenite phase with ferrite phase along with considerable pore formation due to lack of energy input. In the as-built condition of SDSS at higher laser energy density, ferrite is the prevailing phase as seen in Figure 22(g-l). At higher energy density the columnar ferrite grains grow along with austenite grain grow in grain boundary. The austenite grain growth was better observed only on the grain boundary at higher energy density. The further increase in energy density developed mostly ferritic phase in the as built microstructure as shown in figure 22(l). Figure 23 a, b, c shows that the percentage of ferrite increases with increasing laser power and decreases with increasing scan speed and hatch distance. The proportion of the ferrite phase ranges between 45% and 89.7% when different energy densities ranging from 21.4 to 170 J/mm^3 are applied, as shown in Figure 23d. At high laser energy density due to rapid cooling, SDSS produced with LPBF mostly displays a ferritic structure, accounting for about 95% of the composition [12, 40]. The austenite phase in the as-built samples can be efficiently increased to 71% with solution treatment at 1200^{0}C [78].

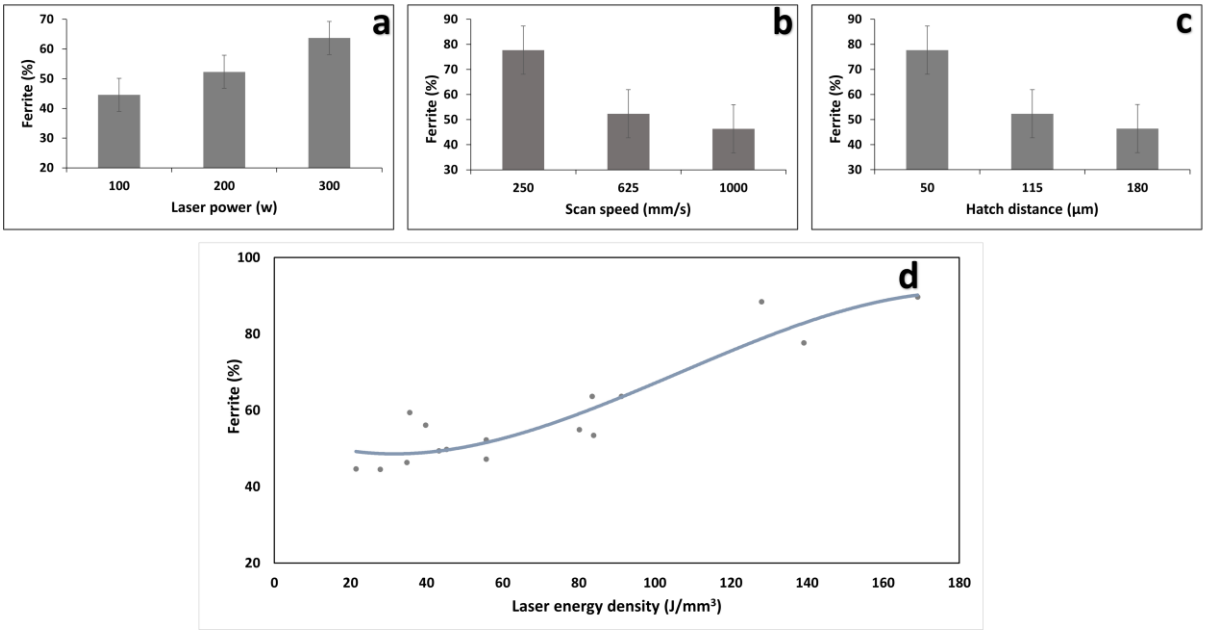

Figure 23. Percentage of ferrite phase in the as-built SAF 2507 samples processed with (a) variation in laser power (w), (b) variation in Scan speed (mm/s), (c) variation in hatch distance (µm), and (d) using different energy density.

To reestablish the equilibrium between austenite and ferrite and hence recover the necessary ductility, post-processing techniques are frequently employed. Reduced solidification speed and improved uniformity of the molten pool, enabling sufficient spreading of the components that stabilize austenite [79].

4.4. Process parameters influence Mechanical properties.

An investigation is conducted to analyse the impact of SLM process parameters on the mechanical characteristics of SAF 2507 samples. This analysis is based on experimental data collected from

the central composite design. The subsequent part will demonstrate the microhardness and tensile behaviour based on the defined SLM process parameters.

4.4.1. Microhardness

Hardness is a fundamental surface property of a material that has significant importance in several manufacturing processes, indicating material ability to withstand plastic deformation or fractures under external forces. This section provides a detailed analysis of how every parameter affects the hardness. This section encompasses the effects of laser power, scan speed, hatch distance, and energy density on Microhardness.

To conduct the analysis on the measured hardness values in relation to the processing parameters, the 15 blocks (Table 8) were produced using various combinations of 3 variables: laser power, scan speed, and hatch distance. The uniformity of the layer thickness (50 μm) across all blocks rendered it unnecessary for inclusion in the analysis. Given the relationship between these process parameters as described in Equation (1), it is anticipated that their impact on the resultant material hardness would be intricate. Hence, this analysis was performed by isolating the impacts of individual process factors, recognizing that the effects of other parameters are hidden inside the individual outcomes. However, this technique allows for the identification of the significant impact of individual process factors.

4.4.1.1. Influences of Laser power on Microhardness

Laser power is the primary process parameter that significantly influences the mechanical properties of SLM objects, as it directly affects the thermal energy generated in each area during a specific period. This, in turn, has a direct impact on the solid-solution aging process of the material. Adjusting the sintering time by varying the laser power in the unit forming area is the main factor influencing the scanning speed. This adjustment directly affects the thermal energy of the pre-alloyed powder and its impact on the solid-solution aging process of the material. Thus, the relationship between laser power and scan speed on material hardness remains steady. The variation of the microhardness value with increasing laser power range from 100 W to 300 W is depicted in Figure 24(a) while maintaining all other parameters at their optimal values (scanning speed: 625 mm/s, hatch spacing: 115 μm).

When the scanning speed and hatch spacing are held constant, Figure 24(a) demonstrates that at low laser power, the pre-alloyed powder in the forming area consumes less energy per unit of time. As a result, a significant portion of the pre-alloyed powder remains partially melted, resulting in an inadequate thermal gradient within the forming layer leading to the formation of numerous pores in the molten channels and pools results in lowering hardness. Lower laser power leads to the formation of narrow radial molten channels with large spacing between adjacent channels (as seen in Figure 22b), as well as elongated longitudinal "perlage" molten pools. These characteristics are attributed to the low surface tension of the molten metal and the shear stress of the solidification phase boundary coupling [80].

As laser power increases, the thermal energy of the pre-alloyed powder in the forming layer becomes sufficient to completely melt. This leads to an improvement in the surface tension within the liquid metal, resulting in the expansion of the radial dimension of the melting channel and the

"perlage" molten pool. Simultaneously, the longitudinal dimensions of the molten pool gradually decrease, eventually transitioning from a lengthwise shape to a wider shape, as depicted in Figure 22g. Subsequently, the number of pores diminishes as the laser power increases, reaching optimal results at a laser power of 200 W, as seen in Figure 15b. The hardness reaches its peak at the laser power of 200 W.

However, if the laser power exceeds the optimal range, the pre-alloyed powder on the forming layer will become more liquid due to the excessive absorption of laser energy per unit time. This leads to an increase in the radial width of the molten pool and molten channel, as well as disorder in their arrangement due to secondary remelting at the boundaries. This will cause it to spread over the adjacent formed layer and the galvanized layer, resulting in varying widths of each melting pool and melting medium as depicted in Figure 22i. According to equation 3, this results in a decrease in hardness. Conversely, the presence of pores is amplified because of the re-melting of the molten channel and molten pool causing reduction in hardness. The correlation between Vickers hardness and grain size is determined by Hall and Petch according to their studies [81].

$$H_v = H_0 + K_H D^{-1/2} \quad \text{.....} \quad \text{equation 3}$$

Where, H_0 and K_H are the respective constants. Hv and D represent the measures of hardness (HV 10) and grain diameter (μm), respectively.

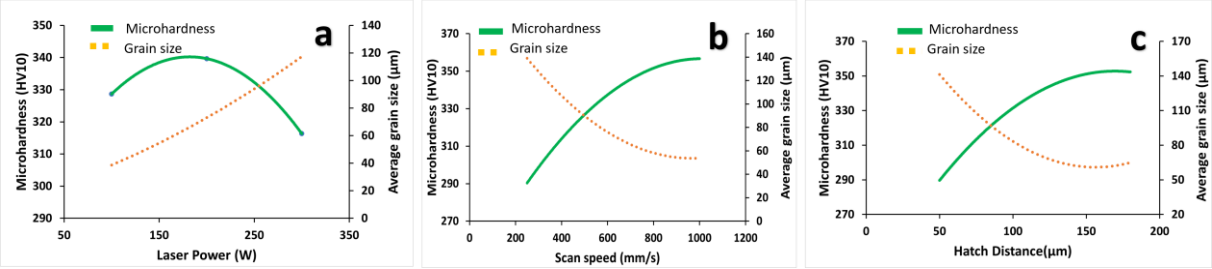

Figure 24: Microhardness of the as-built SAF 2507 samples along the XY-direction; (a) laser power, (b)Scan speed, and (C) Hatch distance.

4.4.1.2. Influences of Scan speed on Microhardness

The hardness values obtained from the measurements are shown in a graphical format, categorized based on the scan speed as seen in Figure 24b. This investigation establishes a direct correlation between hardness and scan speed within the range of 250 mm/s to 1000 mm/s. All variations in hardness associated with different scan speeds are statistically significant. This interaction is related to the microstructure. The laser scanning speed determines the duration of laser energy exposure on the pre-alloyed powder inside the designated forming region, as well as the interval between consecutive laser injection locations. The thermal energy of the pre-alloyed powder may be altered primarily by adjusting the melting time in the unit forming region.

When the hatch spacing and laser power are held constant as medium parameters, Figure 24b shows that at a lower scan speed of 250 mm/s, the grain size expands with increasing laser energy

density, leading to a reduction in hardness. An increase in particle size leads to a reduction in hardness as equation 3 [82]. With an increase in scanning speed, the heat of the pre-alloyed powder in the melting area of the unit gradually decreases, the size of the grains decreases, the molten material takes on a more uniform shape, and the rapid cooling causes a delay in the growth of the matrix grains. This leads to an improved arrangement of the grains and an improvement in hardness. Increasing the scanning speed results in a shorter solidification time for the pre-alloyed powder in the unit melting area due to the reduced scanning time. This is accompanied by smaller dimensions of the molten pools/molten channels, as depicted in Figure 22c. Equation 3 strongly suggests a correlation between hardness and grain size. Smaller grain size leads to increased hardness measurements. High scanning speed leads to a decrease in laser energy input, causing finer and smaller grain structure, and an increase in the microhardness at an energy density of 34.8 J/mm^3. Several PBF systems [83], [84] also show a comparable correlation between scan speed and hardness value.

4.4.1.3. Influences of Hatch spacing on Microhardness

The hatch spacing is the span between the two closest scanning layers. It influences the quality and density of the formed material by affecting the lapping rate, which is the proportion of the width of the molten channel between adjacent pools to the total width of the molten channel.

When the laser power and scan speed are held constant as medium parameters, Figure 24c shows that at a lower hatch distance of 50 μm results in an increase in heat transfer from the adjacent formed portion to the pre-alloyed material at the boundary of the molten pool/molten channel. As illustrated in Figure 22k and in accordance with the direction of the temperature gradient, the boundary portion will increase as the degree of remelting increases, resulting in larger grain sizes and a consistent distribution trend of the molten pool reduces hardness. The samples' reduced hardness can also be attributed to higher particle size from Equation 3.

Figure 24c also demonstrates that a higher hatch spacing results in reduced energy absorption by the pre-alloyed powder on the boundary of the molten pool/molten channel. Consequently, this leads to the formation of a smaller grain size with fine refinement (as seen in 22d) and increases the microhardness of the samples.

4.4.1.4. Influence of overall laser energy density on Microhardness

Figure 25 illustrates the variation of microhardness and average grain size with the variation of laser energy density of the SAF 2507 samples. The microhardness measurements were taken in the XY-direction along various laser energy density. The microhardness values vary from 288 to 357.3 HV. The microhardness profile of SAF 2507 samples shows a good agreement with microstructure and porosity profile size. The highest value of microhardness is achieved at an energy density of 45.2 J/mm3, which is attributed to the smaller grain size. Nevertheless, a considerable quantity of pores is detected at this specific laser energy density of 45.2 J/mm^3.

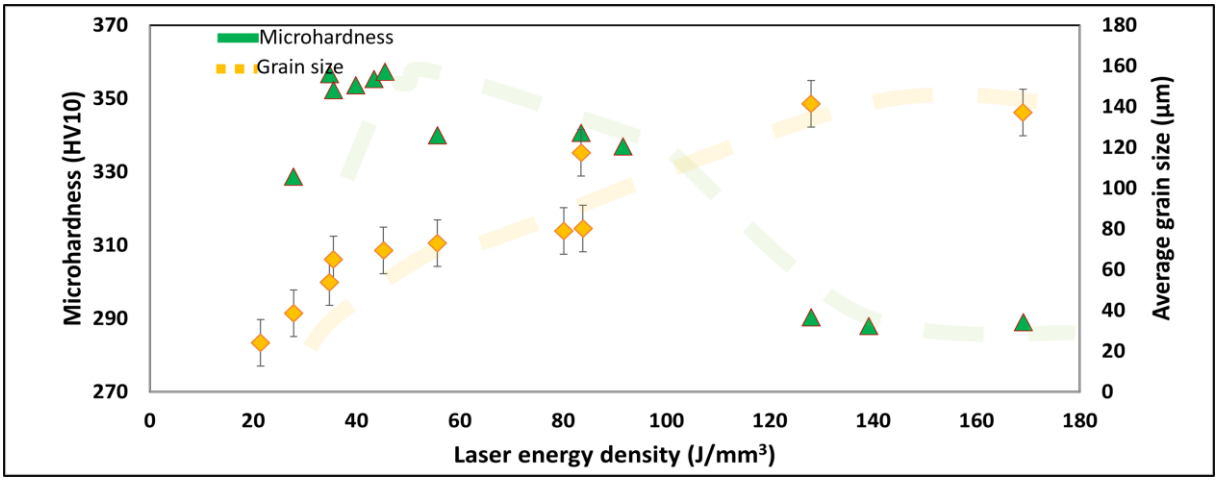

Figure 25. Variation of microhardness with the variation of laser energy density of the as-built SAF 2507 samples along the XY-direction.

The findings also indicate a significant decline in microhardness values with the rise in laser energy density, starting from 55.65 J/mm^3, as seen in Figure 25. This phenomenon can be attributed to the larger size of the grains and the reduced level of grain refining, as described in equation 3.

Figure 26 shows a significant interaction impact among three parameters on microhardness, as illustrated by the interaction plot. In Figure 26a, b, there is an observed correlation between the increase in laser power and the variations in speed and hatch patterns depicted in the interaction plots of (laser power*scan speed) and (laser power*hatch spacing) on microhardness. Figure 26c (scan speed*hatch spacing) plot clearly demonstrates that raising the speed has a noticeable impact on the different hatch curves.

Figure 26a displays the quantitative microhardness (HV 10) data, illustrating the laser power variation for three distinct scan speeds: 402 mm/s, 625 mm/s, and 884 mm/s. These results also demonstrate that for a lower scan speed of 402 mm/s, the keyhole porosity grows in both extent and size as the power increases. This can be attributed to the larger vapor cavity formed at higher laser energy density as shown in Figure 18k. Variation in laser power with higher scanning speed of 848 mm/s results in greater microhardness region.

The microhardness graph is depicted in Figure 26b, demonstrating the variation in laser power for three different hatch spacings: 76.4, 115, and 154 µm. It is seen that higher microhardness is the result of higher hatch spacing combined with higher laser power, whereas increased laser power in conjunction with smaller hatch spacing results in decreased microhardness. A proportionate trend between hatch spacing and scan speed is seen in Figure 26c.

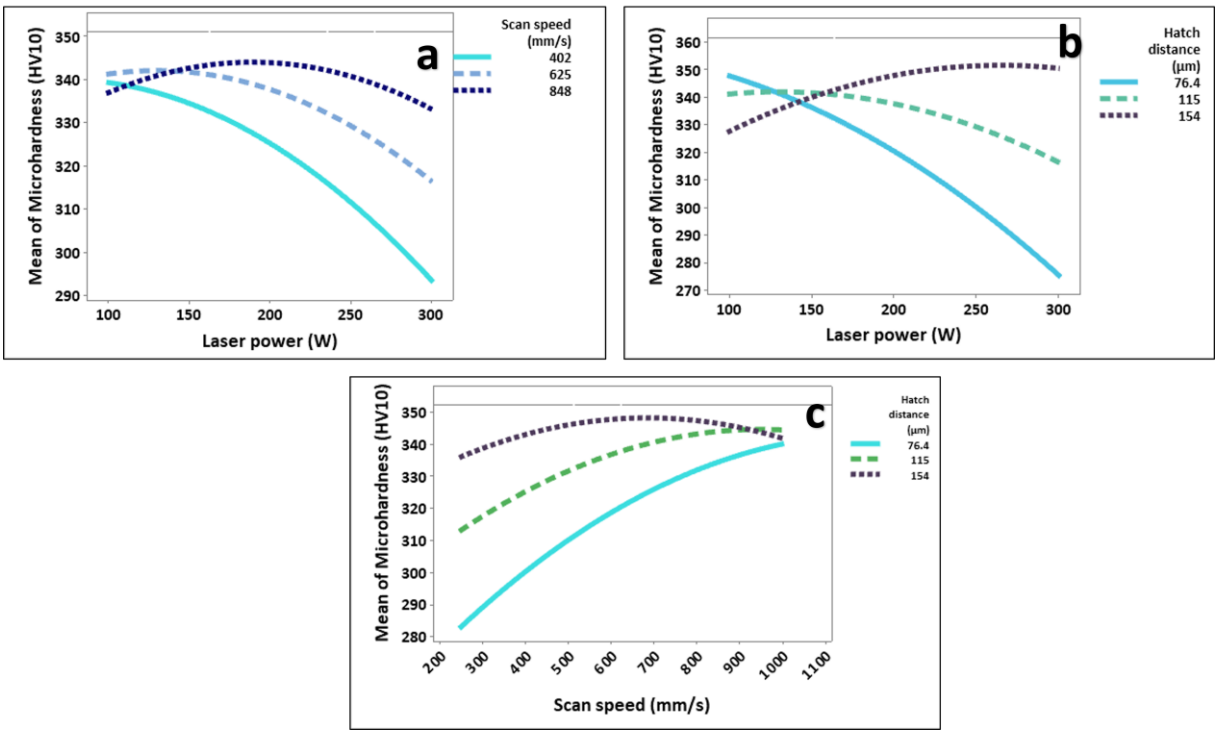

Figure 26. Factor vs. Interaction plots for Microhardness (HV 10), (a) Laser power* Scan speed, (b) Laser power* Hatch speed, and (c) Scan speed * Hatch speed.

The influence of laser power, scan speed, and hatch spacing on the sample microhardness was demonstrated using three-dimensional (3D) surface graphs and the corresponding contour plots shown in Figure 27. Figure 27a, b illustrates the impact of laser power along with scan speed on microhardness at a fixed hatch distance of 115 µm. Higher microhardness is observed when there is a combination of higher laser power and larger scan speed.

The effects of hatch distance and laser power on microhardness are displayed in Figures 27c, d at a fixed scan speed of 625 mm/s. It is seen that increased laser power with reduced hatch spacing results in increased microhardness.

At a fixed laser power of 200 W, Figure 27e, f illustrates how the hatch distance and scan speed affect the resultant microhardness. It is seen that higher microhardness level is produced by lesser scan speeds combined with larger hatch distances.

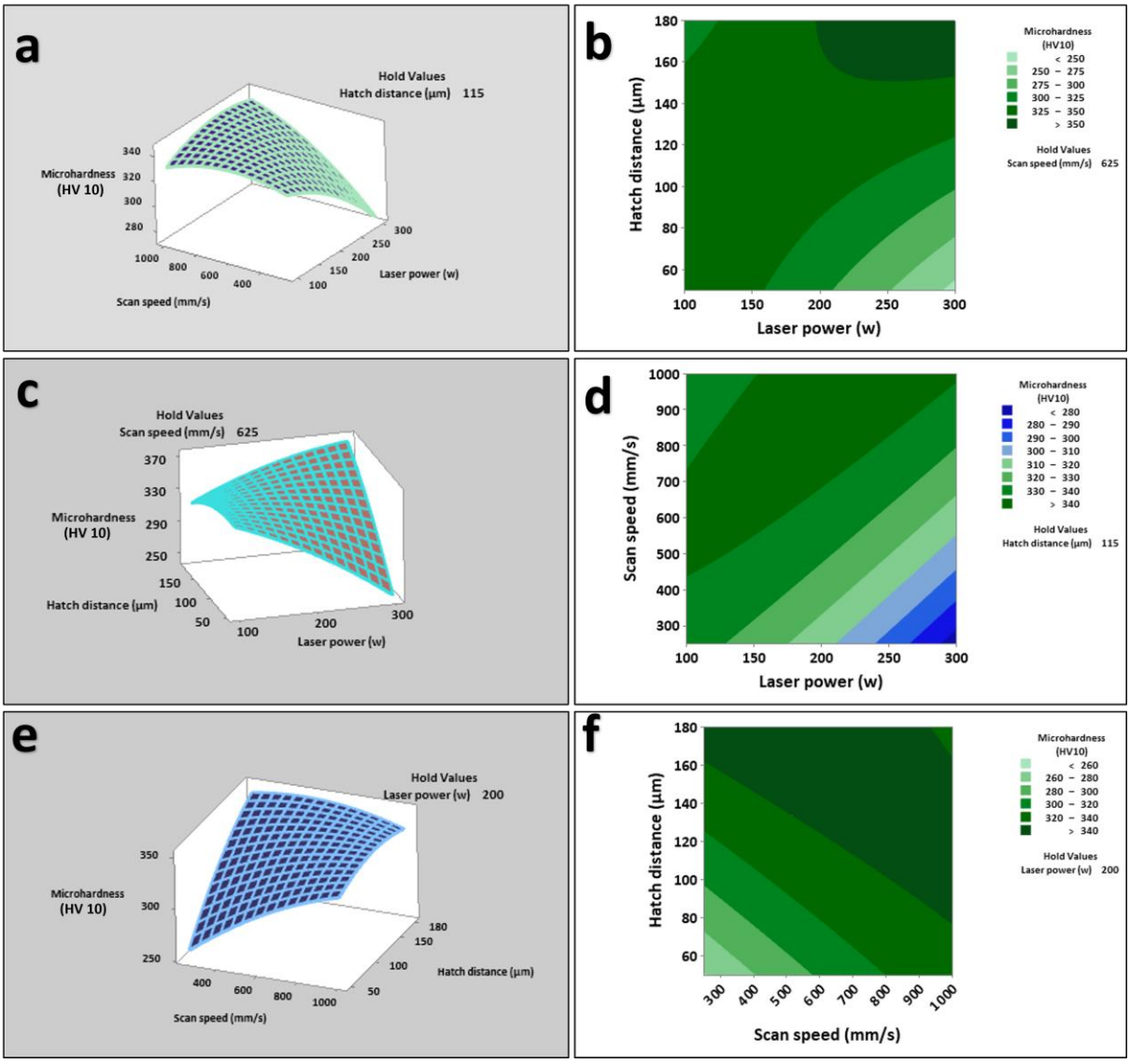

Figure 27. Laser power, scan speed, and hatch distance influence on the Microhardness (HV 10); (a, c, e) surface plots; (b, d, f) counter plots

4.4.2. Tensile Strength Analysis

The tensile strength in powder bed fusion (PBF) is greatly affected by LPBF process parameters. Figures 28a, b depicts the printed tensile samples before and following the tensile test, respectively. Tensile test samples were generated utilizing the set of printing parameters, as illustrated in Table 7. The yield strength (0.2% offset), ultimate tensile strength (UTS), and elongation tensile parameters are determined using different parameter settings.

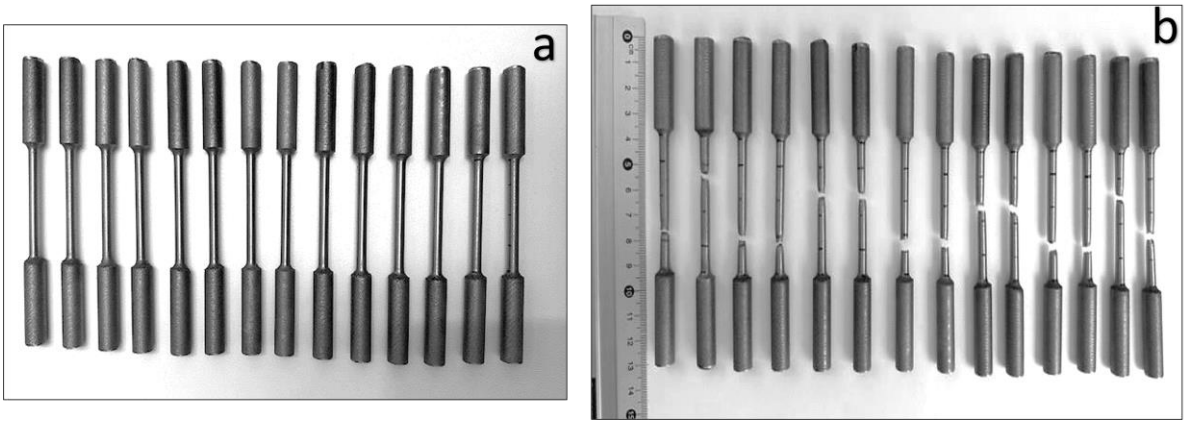

Figure 28. Printed tensile samples using the selected ranges of printing parameters, (a) before tensile test, and (b) after tensile test.

4.4.2.1. Influences of Laser power on Tensile strength

The microstructure of as build sample has a vital role in the mechanical properties in particular; the strength of the component depends on grain size and relative density. The refined grain structure greatly influences the porosity, and strength of the components. Figure 29a displays the engineering stress-strain curves of the printed tensile samples with various laser power. A significant correlation exists between laser power and the ultimate tensile strength, yield strength (0.2% offset), and elongation percentage. Figure 29(b) shows that when the power increases from 200 to 300 W, the ultimate tensile strength reduces gradually from 1139 MPa to 1003 MPa, the yield strength (0.2% offset) decreases gradually from 1012 MPa to 878 MPa, and the elongation increases from 13.4% to 15.1%. Further heat treatment results in an increase in elongation [79].

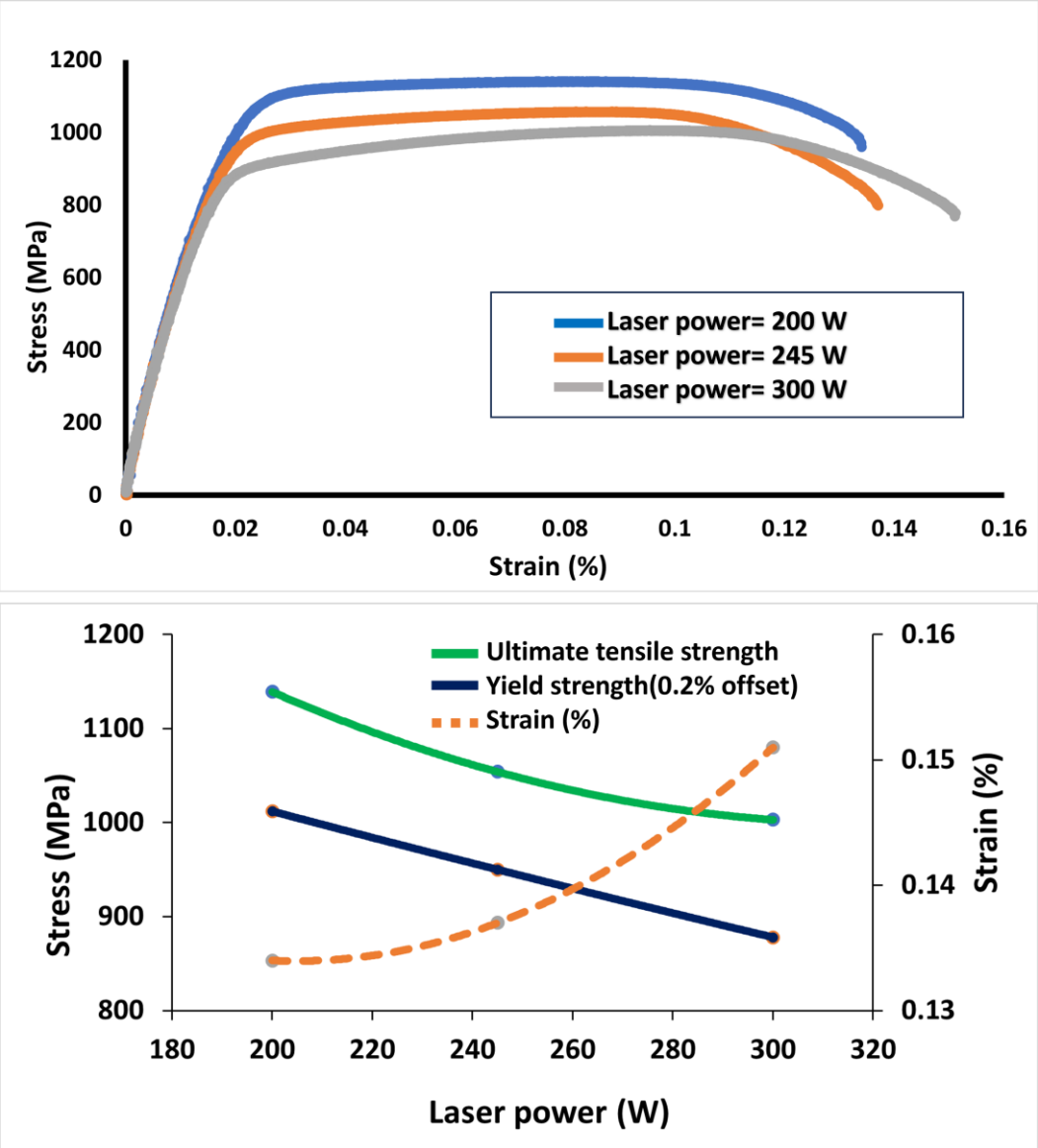

Figure 29(a) Engineering stress-strain curves of printed tensile samples using different laser power, (b) Variation of yield stress (0.2% offset), ultimate tensile strength (UTS), and strain (%) using different laser power.

where the optimum laser power tended to exhibit the highest tensile strength of 1139 MPa. This is attributed to the porosity corresponding to the laser power of 200 W. In laser power of 200 W the porosity of the sample was minimum as seen in figure 15h. On the other hand, the laser power of 200 W generates a finer and more grain refinement as resulting higher UTS and YS value as shown in Figure 22g. Similar trends occur with the yield strength. At laser power of 200 W the yield strength is maximum of 1012 MPa.

4.4.2.2. Influences of Scan speed on Tensile strength

The scanning speed determines the time it takes for the laser to scan and heat the powder, and the time it takes for the workpiece to be formed. When the scanning speed is too low, the forming time of powder melting and sintering is high, and this effect generates keyhole porosity. When the scanning speed increases, the powder forming time is lower and solidification rate is higher resulting in refined grain structure with lowering keyhole porosity. Figure 30a displays the

engineering stress-strain curves of the printed tensile samples with different scan speeds. Figure 30b shows that when the scan speed increases from 402 mm/s to 1000 mm/s, the ultimate tensile strength increases gradually from 1065 MPa to 1304 MPa, the yield strength (0.2% offset) increases gradually from 965 MPa to 1220 MPa, and the elongation decreases from 11.5% to 5.8%. To further enhance the elongation, the material should undergo solution treatment [79].

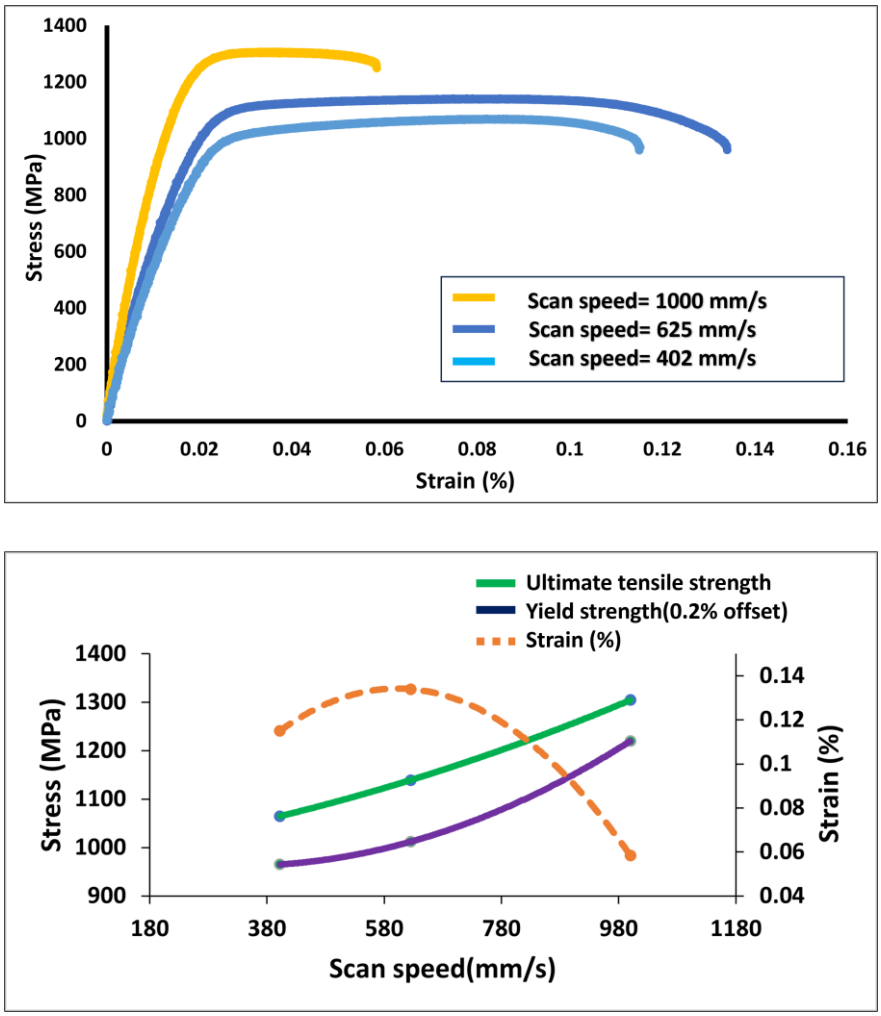

Figure 30.(a) Engineering stress-strain curves of printed tensile samples using different scan speed, (b) Variation of yield stress (0.2% offset), ultimate tensile strength (UTS), and strain (%) using different scan speed.

In figure 30(b) scan speed of 1000mm/s tended to exhibit the highest tensile strength of 1304 MPa. This is attributed to the microstructure corresponding to the scan speed of 1000mm/s. The higher scanning speed creates a small melt pool with lower wetting characteristics, leading to separate solidification, popularly known as the 'balling effect', and a highly porous structure. As seen in figure 22(c), scan speed of 1000mm/s generates a finer and more grain refinement as resulting higher UTS and YS value. Similar trends occur with the yield strength. At the scan speed of 1000mm/s the yield strength is maximum of 1220 MPa. However, at higher scan speed there generates more lack of fusion pores because of improper melting as a result elongation at this scan speed only 5.8%. Further heat treatment results in an increase in elongation [79].

4.4.2.3. Influences of Hatch spacing on Tensile strength

The distance between the centre of two adjacent laser scanning lines is called the hatch spacing. The size of the hatch spacing determines the coincidence degree of the two adjacent laser lines (i.e. the smaller the hatch spacing is, the higher the coincidence degree is.

Figure 31a displays the engineering stress-strain curves of the printed tensile samples with varying hatch distances. Figure 31b shows the influence of hatch spacing on the tensile strength of as build parts. It can be seen from the figure 31b that when the spacing increases from 76 µm, to 180 µm, the ultimate tensile strength gradually increases from 965 MPa to 1292 MPa, the yield strength (0.2% offset) increases gradually from 824 MPa to 1195 MPa, and the elongation decreases from 18.6% to 10.7%.

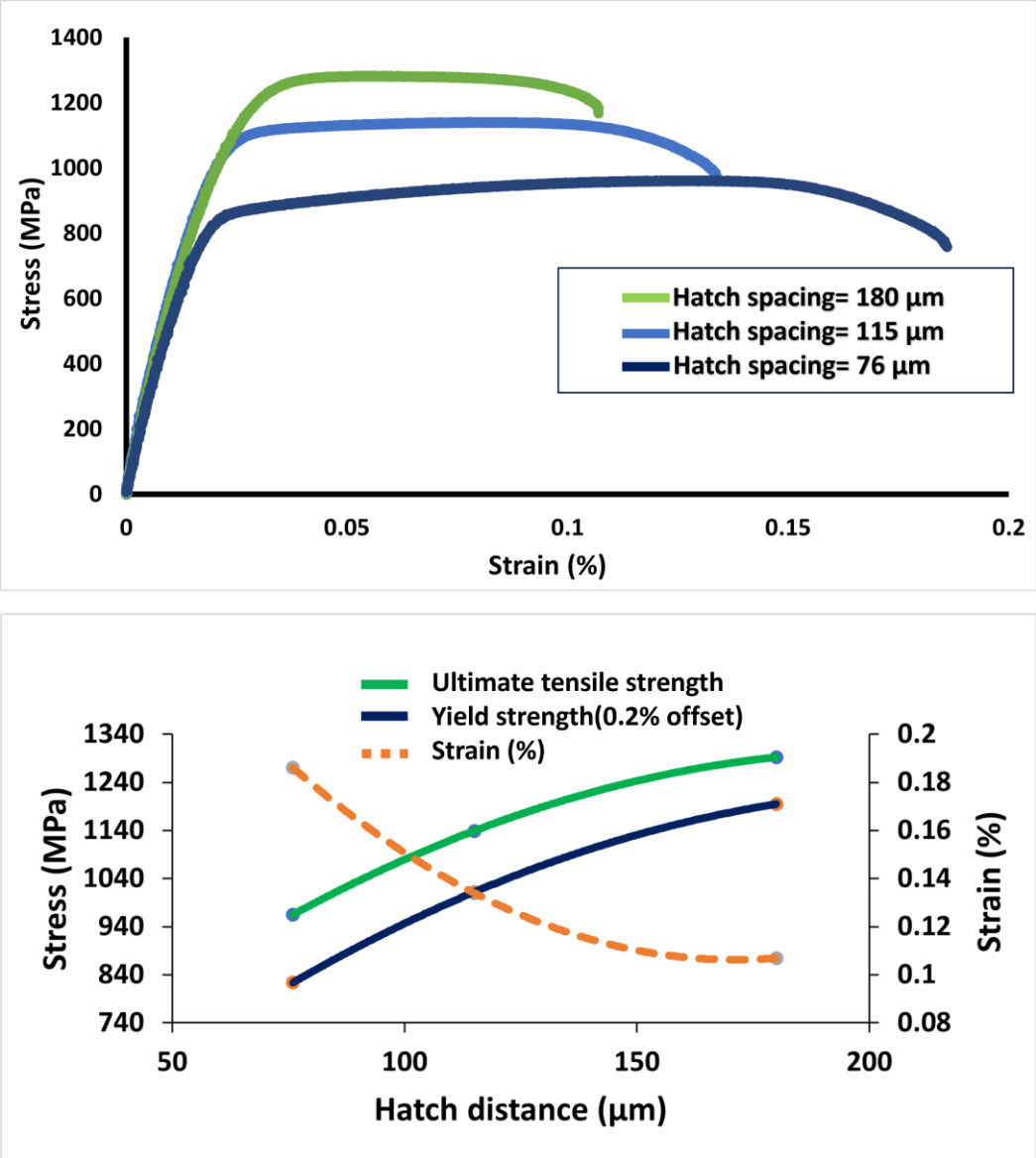

Figure 31. (a) Engineering stress-strain curves of printed tensile samples using different hatch distance, (b) Variation of yield stress (0.2% offset), ultimate tensile strength (UTS), and strain (%) using different hatch distance.

In figure 31(b) Hatch spacing of 180 µm tended to exhibit the highest tensile strength of 1292 MPa. similarly, At the Hatch spacing of 180 µm the yield strength is maximum of 1195 MPa. This is attributed to the microstructure corresponding to the scan speed of hatch spacing of 180 µm. The higher Hatch spacing creates a small melt pool leading to higher solidification rate as seen in figure 22(d).

4.4.2.4. Influences of laser energy density on tensile strength

The yield strength (0.2% offset), ultimate tensile strength (UTS), and elongation tensile parameters are shown in Table 9. The maximum ultimate tensile strength of 1304.522 MPa is obtained when the energy density is 34.8 J/mm^3. This is followed by an energy density of 35.6 J/mm^3, resulting in a tensile strength of 1292.43 MPa. Nevertheless, the energy density of 84.2 J/mm^3 demonstrated the lowest tensile characteristics, with an ultimate strength of 965.21 MPa.

Table 9 presents a comparison between the average tensile characteristics of the printed samples, obtained from the SAF 2507 material, and the DIN EN 10088-3 standard. The LPBF samples exhibited a greater ultimate tensile strength (UTS) of 1304.5 (MPa) together with a reduced elongation of 5.83 %. The observed behaviour can be related to the equilibrium composition of ferritic and austenitic microstructure, as seen in Figure 22c. Kunz et al. [33] observed that LPBF printed samples exhibited comparable mechanical properties, with an ultimate tensile strength (UTS) of 1031 MPa and an elongation of 14%. Furthermore, they observed that the heat-treated samples exhibited a decrease in tensile strength and an increase in elongation (i.e., satisfying the minimal criteria specified by the DIN EN 10088-3 standard).

Table 9. The tensile characteristics of SAF 2507 SDSS for LPBF samples and DIN EN 10088-3 standard [33].

Material	State	Laser energy Density (J/mm^3)	Yield strength (0.2% offset)	Ultimate tensile strength (MPa)	Elongation (%)	Toughness (MJ/m^3)
SAF 2507 SDSS	DIN EN 10088-3 standard		>500	700-900	>25	
	LPBF	34.8	1220	1304	5.83	164
		35.6	1195	1292	10.7	317
		55.6	1012	1139	13.4	345
		68.2	950	1054	13.7	264
		83.5	878	1003	15.1	337
		84.2	824	965	18.6	427
		86.5	965	1064	11.5	272

The effect of various process parameters on the tensile strength of the building part is discussed in the above section. The overall most influencing factor is energy density for SAF 2507, and the maximum UTS and YS value is obtained at an energy density of 34.8 J/mm^3 as shown in Figure 32. This agrees with the microstructure observation, which showed minimum grain size of the as-built SAF 2507 sample.

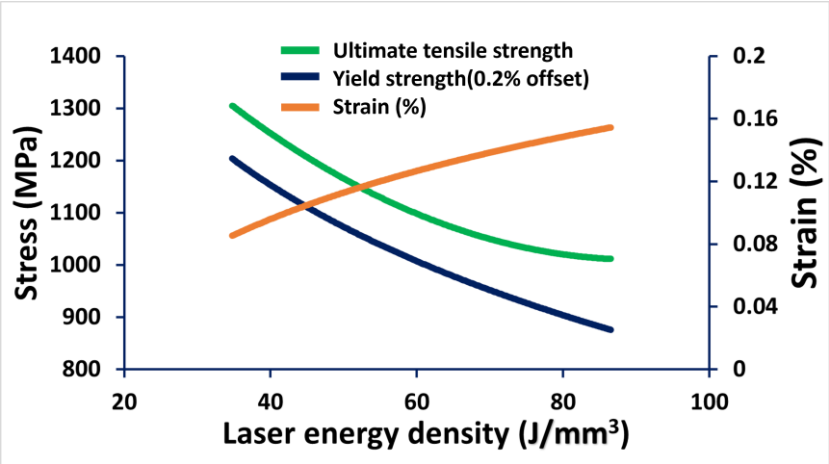

Figure 32. Variation of ultimate tensile strength, yield strength (0.2% offset), and strain (%) of the as-built SAF 2507 samples along different laser energy density.

However, the current results indicate that applying an energy density of 34.8 J/mm^3 is the maximum condition for processing SAF 2507 alloy using a scan speed of 1000 mm/s, 200 W laser power, and 0.115 mm hatch spacing. This could result in better quality of the as-built SAF 2507 parts according to the mutual connection between surface roughness, microstructure, and mechanical properties.

This thesis results reveal that the UTS, YS, and microhardness values are nearly twice as high as those obtained through Forging Processes as seen in Table 10. However, the elongation value is significantly reduced compared to forging processes. Subsequent heat treatment has the potential to enhance elongation to meet the standard requirements. Nevertheless, according to the literature [79], heat treatment decreases the ultimate tensile strength (UTS), yield strength (YS), and microhardness value.

Table 10. Comparison of mechanical properties of conventionally made SDSS [22] and SAF 2507 SDSS produced by LPBF in this work.

Type	UTS (MPa)	YS (MPa)	Microhardness (HV)	Elongation (%) at fracture	Reference
Forging Processes	727.14	522.29	203.93	41.3	[79]
Powder metallurgy (PM)	600-800	400-550	200-250	-	[78]
LPBF (as-build)	1368.6	1162.5	417.13	4.97	[85]
LPBF (as-build with solution-treated at 1000^{0}c)	879.9	621.5	277.17	29.2	
LPBF (as-build with solution-treated at 1200^{0}c)	820.4	564.41	256.63	30.2	

4.4.3. Corrosion properties Analysis

The pitting corrosion test was conducted using ASTM G48, method A. The specimen had a cylindrical shape, measuring 9.72 mm in diameter and 27.2 mm in length, as seen in figure 33. The specimen was produced with an energy density of 55.6 J/mm^3. In this energy density, the porosity of the sample was at its lowest. The mass of the specimen was determined both before and after conducting the pitting corrosion test.

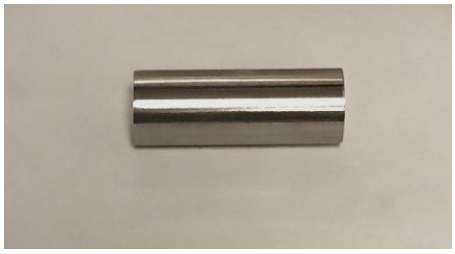

Figure 33. Corrosion test sample

FERRIC CHLORIDE PITTING TEST

Specification: ASTM G48, Method A

Temperature (°C): 22
Time (hour): 24

Laser Energy density (J/mm^3)	Length (cm)	Width (cm)	Surface Area (cm^2)	Initial Weight (g)	Final Weight (g)	Weight Loss (g)	Weight loss per Area (g/cm^2)	Corrosion Rate (µm/y)
55.6	2.73	0.97	9.81	15.62295	15.6203	0.00655	0.00027	127.65

Figure 34. Corrosion test Report.

The test specimen was polished with a P220, P1200, and P2400 grits finish and rinsed in an ultrasonic cleaner to remove any debris. It was passivated for 24 hours before being placed into the test solution. The test solution is formulated following the guidelines of ASTM G48 Method A. The solution and bath water were preserved at a temperature of 22°C. Figure 29 illustrates that the samples produced at a printing density of 55.6 J/mm^3 had a corrosion rate of 127.65 µm/year. Corresponding findings can be observed in the literature [75].

Chapter 5

Conclusion

The present investigation concentrated on examining the impact of LPBF process parameters on the microstructure and mechanical characteristics of the as-built SAF 2507 samples. An analysis was conducted on the microstructure and mechanical properties of these components across a range of chosen SLM parameters settings using DoE. The impact of Laser powder-bed fusion parameters, including laser power, hatch spacing, and scanning speed, on the characteristics of the as built samples is discussed. Every parameter has an impact on the porosity, microstructure, tensile strength, hardness, and corrosion characteristics of the manufactured samples. Each parameter is thoroughly examined, and the key findings are described as follows.

1. Porosity develops within the SAF 2507 samples throughout the manufacturing process. The size and distribution of this porosity differ according to the parameters of the LPBF process. The porosity level achieved its lowest value of 0.024% when the laser power was set to 200 W, the scan speed was set to 625 mm/s, and the hatch spacing was set to 115 µm. In addition, the energy density was 55.6 J/mm^3. At lower energy densities, the presence of lack of fusion porosity is the prevailing factor. Conversely, keyhole porosity arises when circumstances with greater energy density. The optimum energy density range that yields the porosity below 1% and circularity of pores over 0.90 is from 34.8 J/mm^3 to 83.8 J/mm^3. Applying a solution treatment can effectively decrease the porosity of the as-built samples.

2. The microstructure of the SAF 2507 samples exhibits significant changes when exposed to different LPBF process parameters and energy densities. At lower energy density, the austenite phase and the ferrite phase exist in almost equal proportions. The ferrite phase becomes dominant after the laser energy density exceeds 45.2 J/mm^3 and becomes 89% at an energy density of 170 J/mm^3. The austenite phase in the as-built samples may be efficiently increased to 71% with solution treatment at 1200^{0}C. Furthermore, enhancing the rate at which solidification occurs and achieved more consistency in the molten pool, facilitating adequate dispersion of the elements that maintain the stability of austenite.

3. The grain size of the SAF 2507 samples increases proportionally to the energy density. The generation of an equiaxed grain structure and the uniformity of the microstructure in the as build samples range from 21.4 to 45.2 J/mm^3 along the XY plane.

4. The microhardness of SAF 2507 samples is examined using different process parameters settings. It is seen that the microhardness of SAF 2507 samples is consistent with the microstructure studies made along the XY plane. Nevertheless, the microhardness of SAF 2507 samples is influenced by pre-existing porosity. The as-built sample of SAF 2507 samples has a hardness value ranging from 288 HV to 357 HV, which is nearly twice as high as those obtained through Forging Processes. The energy density required for achieving improved hardness in the as-built sample ranges from 27.83 J/mm^3 to 91.57 J/mm^3. Utilizing different grain refining processes can enhance the hardness of a sample in its original state.

5. The investigation focuses on the UTS, YS, elongation, and toughness properties of the SAF 2507 samples, specifically in relation to varying LPBF process parameters. The UTS, and YS of SAF 2507 samples were determined and found within the range of 965 MPa to 1304 MPa and 824 MPa to 1220 MPa, respectively. The toughness value of SAF 2507 samples found within the range of 164 to 427 MJ/m^3**.** These values were obtained for energy densities ranging from 34.8 J/mm^3 to 86.5 J/mm^3. The highest recorded UTS, and YS are 1304 MPa, and 1220 MPa respectively, when the energy density was 34.8 J/mm^3. The highest value of toughness observed was 427 MJ/m^3 at an energy density of 84.2 J/mm^3. The maximum elongation is 18.6%, achieved at an energy density of 84.28 J/mm^3. However, further heat treatment is necessary to improve elongation.

6. A corrosion rate of 127.65 µm/year is achieved with the sample of least porosity, produced with an energy density of 55.6 J/mm^3. The SAF 2507 sample offers higher corrosion resistance.

Recommendations

The thesis aims to address the research gap in LPBF fabrication of SAF 2507. This research has established an empirical correlation by correlating the changes in the microstructure and mechanical properties of LPBF fabricated SAF 2507 SDSS with the LPBF process parameters. This was accomplished by conducting a study of porosity, microhardness, tensile strength, and corrosion rate calculation using various combinations of parameters. Moreover, it offers a promising chance to enhance research in the fabrication of SAF 2507 using LPBF technology. Furthermore, it provides the following research opportunities for manufacturing of SAF 2507 SDSS using LPBF:

1. The SAF 2507 SDSS can be printed using various layer thicknesses and hatch strategies. This will offer information regarding the influence of these parameters on microstructure and mechanical properties.

2. The lack of the austenite phase was seen in the as-printed samples when subjected to greater energy density. Several heat treatment analyses can be performed to restore the austenite phase.

3. The elongation percentage in the printed samples is below the standard. Heat treatment can be applied to enhance the level of elongation (%).

4. Corrosion samples can be printed using different parameter settings to observe the impact of processing parameters on the corrosion rate. This research is currently in progress.

List of References

[1] M. Mehrpouya *et al.*, "The potential of additive manufacturing in the Smart Factory Industrial 4.0: A Review," *Applied Sciences*, vol. 9, no. 18, p. 3865, Sep. 2019. doi:10.3390/app9183865

[2] "ASM Handbooks Online." https://www.researchgate.net/publication/33514539_ASM_Handbooks_Online (accessed Dec. 29, 2023).

[3] M. Bogers and W. Horst, "Collaborative prototyping: Cross-fertilization of knowledge in prototype-driven problem solving," *J. Prod. Innov. Manag.*, vol. 31, no. 4, pp. 744–764, 2014, doi: 10.1111/JPIM.12121.

[4] S. Nath, Process-property-microstructure relationships in laser-powder bed fusion of 420 stainless steel. doi:10.18297/etd/3074

[5] A study of the state-of-the-art rapid prototyping technologies ..., https://www.proquest.com/openview/c5693ea218c0a906e8d1a3b150d141b7/1?pq-origsite=gscholar&cbl=2044010 (accessed Feb. 15, 2024).

[6] F. Hengsbach et al., "Duplex stainless steel fabricated by selective laser melting - microstructural and mechanical properties," Materials & Design, vol. 133, pp. 136–142, 2017. doi: 10.1016/j.matdes.2017.07.046

[7] G. Chail and P. Kangas, "Super and Hyper Duplex Stainless Steels: Structures, properties and applications," Procedia Structural Integrity, vol. 2, pp. 1755–1762, 2016. doi: 10.1016/j.prostr.2016.06.221.

[8] "Duplex stainless steels microstructure, properties and applications," *Anti-Corrosion Methods and Materials*, vol. 45, no. 2, 1998. doi: 10.1108/acmm.1998.12845bae.001

[9] S. Krasnorutskyi, H. Pries, M. Zinke, and D. Keil, "Metallurgical influence of multibeam technology on duplex stainless-steel welds," *Weld. World*, vol. 57, no. 4, pp. 487–494, Jul. 2013, doi: 10.1007/S40194-013-0042-6.

[10] A. Bautista, G. Blanco, and F. Velasco, "Corrosion behaviour of low-nickel austenitic stainless steels reinforcements: A comparative study in simulated pore solutions," *Cem. Concr. Res.*, vol. 36, no. 10, pp. 1922–1930, Oct. 2006, doi: 10.1016/J.CEMCONRES.2005.10.009.

[11] Md. H. Ali, N. Sabyrov, and E. Shehab, "Powder Bed Fusion–laser melting (PBF–LM) process: Latest review of materials, process parameter optimization, application, and up-to-date innovative technologies," *Progress in Additive Manufacturing*, vol. 7, no. 6, pp. 1395–1422, May 2022. doi:10.1007/s40964-022-00311-9

[12] P. A. Hooper, "Melt pool temperature and cooling rates in laser powder bed fusion," *Additive Manufacturing*, vol. 22, pp. 548–559, 2018. doi: 10.1016/j.addma.2018.05.032

[13] H. Irrinki, *Material-process-property relationships of 17-4 stainless steel fabricated by laser-powder bed fusion followed by hot isostatic pressing.* doi:10.18297/etd/3024

[14] K. P. Davidson and S. B. Singamneni, "Metallographic evaluation of duplex stainless-steel powders processed by selective laser melting," *Rapid Prototyping Journal*, vol. 23, no. 6, pp. 1146–1163, 2017. doi:10.1108/rpj-04-2016-0053

[15] K. Chan and S. Tjong, "Effect of secondary phase precipitation on the corrosion behavior of Duplex Stainless Steels," *Materials*, vol. 7, no. 7, pp. 5268–5304, Jul. 2014. doi:10.3390/ma7075268

[16] L. Weber and P. J. Uggowitzer, "Partitioning of chromium and molybdenum in super duplex stainless steels with respect to nitrogen and nickel content," *Mater. Sci. Eng. A*, vol. 242, no. 1–2, pp. 222–229, 1998, doi: 10.1016/S0921-5093(97)00521-2.

[17] H. Y. Liou, R. I. Hsieh, and W. T. Tsai, "Microstructure and stress corrosion cracking in simulated heat-affected zones of duplex stainless steels," *Corros. Sci.*, vol. 44, no. 12, pp. 2841–2856, Dec. 2002, doi: 10.1016/S0010-938X(02)00068-9.

[18] C. Sommariva, D. Pinciroli, E. Tolle, and R. Adinolfi, "Optimization of material selection for evaporative desalination plants in order to achieve the highest cost-benefit ratio," *Desalination*, vol. 124, no. 1–3, pp. 99–103, Nov. 1999, doi: 10.1016/S0011-9164(99)00093-4.

[19] D. C. Agarwal, "DUPLEX STAINLESS STEELS THE COST EFFECTIVE ANSWER TO CORROSION PROBLEMS OF MAJOR INDUSTRIES.," *Key Eng. Mater.*, vol. 20–28, no. pt 1-4, 1987, doi: 10.4028/WWW.SCIENTIFIC.NET/KEM.20-28.1677.

[20] P. Paulraj and R. Garg, "EFFECT OF INTERMETALLIC PHASES ON CORROSION BEHAVIOR AND MECHANICAL PROPERTIES OF DUPLEX STAINLESS STEEL AND SUPER-DUPLEX STAINLESS STEEL," *Adv. Sci. Technol. Res. J.*, vol. 9, pp. 87–105, 2015, doi: 10.12913/22998624/59090.

[21] X. Zhang *et al.*, "Microstructure and mechanical properties of top-tig-wire and arc additive manufactured super duplex stainless steel (ER2594)," *Materials Science and Engineering: A*, vol. 762, p. 138097, Aug. 2019. doi: 10.1016/j.msea.2019.138097

[22] Arumugham Akilan, A. (no date) *Properties of 25cr7ni stainless steel fabricated through laser-powder bed fusion.* [Preprint]. doi:10.18297/etd/3803.

[23] J. H. Lee, C. M. Lee, and D. H. Kim, "Repair of damaged parts using wire arc additive manufacturing in machine tools," *J. Mater. Res. Technol.*, vol. 16, pp. 13–24, Jan. 2022, doi: 10.1016/J.JMRT.2021.11.156.

[24] C. Y. Yap *et al.*, "Review of selective laser melting: Materials and applications," *Appl. Phys. Rev.*, vol. 2, no. 4, Dec. 2015, doi: 10.1063/1.4935926.

[25] H. Rezaeifar and M. Elbestawi, "Porosity Formation mitigation in laser powder bed fusion process using a control approach," *Optics & Laser Technology*, vol. 147, p. 107611, Mar. 2022. doi:10.1016/j.optlastec.2021.107611

[26] M. R. Stoudt, R. E. Ricker, E. A. Lass, and L. E. Levine, "Influence of Postbuild Microstructure on the Electrochemical Behavior of Additively Manufactured 17-4

PH Stainless Steel," *JOM*, vol. 69, no. 3, pp. 506–515, Mar. 2017, doi: 10.1007/S11837-016-2237-Y.

[27] U. Kamachi Mudali, A. K. Bhaduri, and J. B. Gnanamoorthy, "Localised corrosion behaviour of 17–4 PH stainless steel," *Mater. Sci. Technol.*, vol. 6, no. 5, pp. 475–481, Feb. 2012, doi: 10.1179/026708390790190856.

[28] S. Feng *et al.*, "Novel ferritic stainless steel with advanced mechanical properties and significant magnetic responses processed by selective laser melting," *Mater. Trans.*, vol. 60, no. 6, pp. 1096–1102, 2019, doi: 10.2320/MATERTRANS.M2018374.

[29] F. Hengsbach *et al.*, "Duplex stainless steel fabricated by selective laser melting - Microstructural and mechanical properties," *Mater. Des.*, vol. 133, pp. 136–142, Nov. 2017, doi: 10.1016/J.MATDES.2017.07.046.

[30] M. Knyazeva and M. Pohl, "Duplex Steels. Part II: Carbides and Nitrides," *Metallogr. Microstruct. Anal.*, vol. 2, no. 5, pp. 343–351, Oct. 2013, doi: 10.1007/S13632-013-0088-2.

[31] M. Piras, A. Hor, and E. Charkaluk, "Control of the microstructure and mechanical properties of a super duplex SAF 2507 steel produced by Additive Manufacturing," *Lecture Notes in Mechanical Engineering*, pp. 1–9, Nov. 2023. doi:10.1007/978-3-031-47784-3_1

[32] K. P. Davidson and S. B. Singamneni, "Metallographic evaluation of duplex stainless-steel powders processed by selective laser melting," *Rapid Prototyp. J.*, vol. 23, no. 6, pp. 1146–1163, 2017, doi: 10.1108/RPJ-04-2016-0053.

[33] J. Nowacki and A. Łukojć, "Structure and properties of the heat-affected zone of duplex steels welded joints," *J. Mater. Process. Technol.*, vol. 164–165, pp. 1074–1081, May 2005, doi: 10.1016/J.JMATPROTEC.2005.02.243.

[34] T. H. Chen and J. R. Yang, "Microstructural characterization of simulated heat affected zone in a nitrogen-containing 2205 duplex stainless steel," *Mater. Sci. Eng. A*, vol. 338, no. 1–2, pp. 166–181, Dec. 2002, doi: 10.1016/S0921-5093(02)00065-5.

[35] Standard terminology for additive manufacturing TECHNOLOGIES1,2, http://web.mit.edu/2.810/www/files/readings/AdditiveManufacturingTerminology.pdf (accessed Aug. 26, 2023).

[36] S. Saleh Alghamdi, S. John, N. Roy Choudhury, and N. K. Dutta, "Additive Manufacturing of Polymer Materials: Progress, promise and challenges," *Polymers*, vol. 13, no. 5, p. 753, 2021. doi:10.3390/polym13050753

[37] E. Yasa, "Selective Laser melting," *Additive Manufacturing*, pp. 77–120, 2021. doi:10.1016/b978-0-12-818411-0.00017-3

[38] D. Dev Singh, T. Mahender, and A. Raji Reddy, "Powder Bed Fusion Process: A Brief Review," *Materials Today: Proceedings*, vol. 46, pp. 350–355, 2021. doi: 10.1016/j.matpr.2020.08.415

[39] R. Singh *et al.*, "Powder bed fusion process in Additive Manufacturing: An overview," *Materials Today: Proceedings*, vol. 26, pp. 3058–3070, 2020. doi: 10.1016/j.matpr.2020.02.635

[40] T. Maconachie *et al.*, "SLM lattice structures: Properties, performance, applications and challenges," *Materials & Design*, vol. 183, p. 108137, Dec. 2019. doi: 10.1016/j.matdes.2019.108137

[41] F. Calignano, T. Tommasi, D. Manfredi, and A. Chiolerio, "Additive Manufacturing of a microbial fuel cell—a detailed study," *Scientific Reports*, vol. 5, no. 1, 2015. doi:10.1038/srep17373

[42] W. O'Neill, C. J. Sutcliffe, R. Morgan, A. Landsborough, and K. K. B. Hon, "Investigation on multi-layer direct metal laser sintering of 316L Stainless Steel Powder Beds," *CIRP Annals*, vol. 48, no. 1, pp. 151–154, 1999. doi:10.1016/s0007-8506(07)63153-9

[43] I. Yadroitsev, I. Yadroitsava, P. Bertrand, and I. Smurov, "Factor analysis of selective laser melting process parameters and geometrical characteristics of synthesized single tracks," *Rapid Prototyping Journal*, vol. 18, no. 3, pp. 201–208, 2012. doi:10.1108/13552541211218117

[44] Gu H, Gong H, Pal D, Rafi K, Starr T, and Stucker B (2013) Influences of energy density on porosity and microstructure of selective laser melted 17-4PH stainless steel. *Proceedings of Solid Freeform Fabrication Symposium*, 474–489.(not IEE style)

[45] S. Dingal, T. R. Pradhan, J. K. Sundar, A. R. Choudhury, and S. K. Roy, "The application of Taguchi's method in the experimental investigation of the Laser Sintering Process," *The International Journal of Advanced Manufacturing Technology*, vol. 38, no. 9–10, pp. 904–914, 2007. doi:10.1007/s00170-007-1154-1

[46] E. Abele, H. A. Stoffregen, M. Kniepkamp, S. Lang, and M. Hampe, "Selective laser melting for manufacturing of thin-walled porous elements," *Journal of Materials Processing Technology*, vol. 215, pp. 114–122, 2015. doi: 10.1016/j.jmatprotec.2014.07.017

[47] C. Qiu, N. J. E. Adkins, and M. M. Attallah, "Microstructure and tensile properties of selectively laser-melted and of HIPed laser-melted ti–6al–4v," *Materials Science and Engineering: A*, vol. 578, pp. 230–239, 2013. doi:10.1016/j.msea.2013.04.099

[48] K. Kempen, E. Yasa, L. Thijs, J.-P. Kruth, and J. Van Humbeeck, "Microstructure and mechanical properties of selective laser melted 18ni-300 steel," *Physics Procedia*, vol. 12, pp. 255–263, 2011. doi:10.1016/j.phpro.2011.03.033 B.

[49] J. Sun, Y. Yang, and D. Wang, "Parametric optimization of selective laser melting for forming ti6al4v samples by Taguchi Method," *Optics & Laser Technology*, vol. 49, pp. 118–124, 2013. doi:10.1016/j.optlastec.2012.12.002

[50] J. Delgado, J. Ciurana, and C. A. Rodríguez, "Influence of process parameters on part quality and mechanical properties for DMLS and SLM with iron-based materials," *The International Journal of Advanced Manufacturing Technology*, vol. 60, no. 5–8, pp. 601–610, 2011. doi:10.1007/s00170-011-3643-5

[51] Vandenbroucke and J. Kruth, "Selective laser melting of biocompatible metals for rapid manufacturing of medical parts," *Rapid Prototyping Journal*, vol. 13, no. 4, pp. 196–203, 2007. doi:10.1108/13552540710776142

[52] Liu B, Wildman R, Tuck C, Ashcroft I, Hague R, (2011) Investigation the effect of particle size distribution on processing parameters optimisation in selective laser melting process. *Proceedings of Solid Freeform Fabrication Symposium*, 227–238(not IEE style)

[53] B. Song, S. Dong, P. Coddet, H. Liao, and C. Coddet, "Fabrication of NICR alloy parts by selective laser melting: Columnar microstructure and anisotropic mechanical behavior," *Materials & Design*, vol. 53, pp. 1–7, 2014. doi:10.1016/j.matdes.2013.07.010

[54] S. Li *et al.*, "Effect of layer thickness on the melt pool behavior and pore defects evolution of selective laser melting cucrzr alloy," *Journal of Alloys and Compounds*, vol. 967, p. 171778, Dec. 2023. doi:10.1016/j.jallcom.2023.171778

[55] A. Mouritz, Introduction to aerospace materials, 2012. doi:10.2514/4.869198

[56] Z. Li *et al.*, "First-principles study of mechanical and thermodynamic properties of intermetallic Pt3M (M = Al, Hf, Zr, Co, Y, Sc)," *Comput. Condens. Matter*, vol. 23, Jun. 2020, doi: 10.1016/J.COCOM.2020.E00462.

[57] V. Selvamanickam, "Engineering REBCO high temperature superconductor materials for applications," *Phys. C Supercond. its Appl.*, vol. 614, Nov. 2023, doi: 10.1016/J.PHYSC.2023.1354355.

[58] S. Ayadi and A. Hadji, "Effect of heat treatments on the microstructure and wear resistance of a modified hadfield steel," *Metallofiz. i Noveishie Tekhnologii*, vol. 41, no. 5, pp. 607–620, 2019, doi: 10.15407/MFINT.41.05.0607.

[59] D. K. Ganji and G. Rajyalakshmi, "Influence of Alloying Compositions on the Properties of Nickel-Based Superalloys: A Review," *Lect. Notes Mech. Eng.*, pp. 537–555, 2020, doi: 10.1007/978-981-15-1071-7_44/COVER.

[60] M. Okayasu and D. Ishida, "Effect of microstructural characteristics on mechanical properties of austenitic, ferritic, and γ-α duplex stainless steels," *Metallurgical and Materials Transactions A*, vol. 50, no. 3, pp. 1380–1388, Jan. 2019. doi:10.1007/s11661-018-5083-4

[61] D. S. D. Kahar, "Duplex Stainless Steels-An overview," *Int. J. Eng. Res. Appl.*, vol. 07, no. 04, pp. 27–36, Apr. 2017, doi: 10.9790/9622-0704042736.

[62] Y. R. Yoo, S. G. Jang, K. T. Oh, J. G. Kim, and Y. S. Kim, "Influences of passivating elements on the corrosion and biocompatibility of super stainless steels," *J. Biomed. Mater. Res. - Part B Appl. Biomater.*, vol. 86, no. 2, pp. 310–320, Aug. 2008, doi: 10.1002/JBM.B.31018.

[63] I. Alvarez-Armas, "Duplex Stainless Steels: Brief History and Some Recent Alloys," *Recent Patents Mech. Eng.*, vol. 1, no. 1, pp. 51–57, Jan. 2010, doi: 10.2174/1874477X10801010051.

[64] https://www.corrotherm.co.uk/hubfs/resources/corrotherm-introduction-super-duplex-stainless-steels.pdf

[65] G. N. Nigon, O. Burkan Isgor, and S. Pasebani, "The effect of annealing on the selective laser melting of 2205 duplex stainless steel: Microstructure, grain orientation, and manufacturing challenges," *Opt. Laser Technol.*, vol. 134, Feb. 2021, doi: 10.1016/J.OPTLASTEC.2020.106643.

[66] A. Mulhi, S. Dehgahi, P. Waghmare, and A. J. Qureshi, "Process parameter optimization of 2507 super duplex stainless steel additively manufactured by the laser powder bed fusion technique," *Metals*, vol. 13, no. 4, p. 725, 2023. doi:10.3390/met13040725

[67] M. L. Gatto *et al.*, "The potential of duplex stainless steel processed by laser powder bed fusion for biomedical applications: A Review," *Metals*, vol. 13, no. 5, p. 949, 2023. doi:10.3390/met13050949

[68] C. Xie *et al.*, *Study on the effect of solution treatment on mechanical and corrosion properties of SAF 2507dss produced by SLM*, 2023. doi:10.2139/ssrn.4451031

[69] *Test methods for pitting and crevice corrosion resistance of stainless steels and related alloys by use of ferric Chloride Solution*. doi:10.1520/g0048-11

[70] J. Metelkova *et al.*, "On the influence of laser defocusing in Selective Laser Melting of 316L," *Additive Manufacturing*, vol. 23, pp. 161–169, 2018. doi:10.1016/j.addma.2018.08.006
[71] A. du Plessis, "Effects of process parameters on porosity in laser powder bed fusion revealed by X-ray tomography," *Additive Manufacturing*, vol. 30, p. 100871, Dec. 2019. doi:10.1016/j.addma.2019.100871
[72] R. Chai, Y. Zhang, B. Zhong, and C. Zhang, "Effect of scan speed on grain and microstructural morphology for laser additive manufacturing of 304 Stainless Steel," *REVIEWS ON ADVANCED MATERIALS SCIENCE*, vol. 60, no. 1, pp. 744–760, Jan. 2021. doi:10.1515/rams-2021-0068
[73] Z. Dong, Y. Liu, W. Wen, J. Ge, and J. Liang, "Effect of hatch spacing on melt pool and as-built quality during selective laser melting of stainless steel: Modeling and experimental approaches," *Materials*, vol. 12, no. 1, p. 50, Dec. 2018. doi:10.3390/ma12010050
[74] Q. S. Wei *et al.*, "Effects of the processing parameters on the forming quality of stainless steel parts by selective laser melting," *Advanced Materials Research*, vol. 189–193, pp. 3668–3671, Feb. 2011. doi:10.4028/www.scientific.net/amr.189-193.3668
[75] M. Gor *et al.*, "A critical review on effect of process parameters on mechanical and microstructural properties of powder-bed fusion additive manufacturing of SS316L," *Materials*, vol. 14, no. 21, p. 6527, Oct. 2021. doi:10.3390/ma14216527
[76] M. L. Gatto *et al.*, "The potential of duplex stainless steel processed by laser powder bed fusion for biomedical applications: A Review," *Metals*, vol. 13, no. 5, p. 949, May 2023. doi:10.3390/met13050949
[77] N. Haghdadi *et al.*, "On the pitting corrosion of 2205 duplex stainless steel produced by laser powder bed fusion additive manufacturing in the as-built and post-processed conditions," *Materials & Design*, vol. 212, p. 110260, Dec. 2021. doi:10.1016/j.matdes.2021.110260
[78] P. Kangas and G. C. Chai, "Use of advanced austenitic and duplex stainless steels for applications in oil & gas and process industry," *Adv. Mater. Res.*, vol. 794, pp. 645–669, 2013, doi: 10.4028/WWW.SCIENTIFIC.NET/AMR.794.645.
[79] L. Karlsson, "Welding duplex stainless steels - A review of current recommendations," *Weld. World*, vol. 56, no. 5–6, pp. 65–76, 2012, doi: 10.1007/BF03321351.
[80] N. Haghdadi, P. Cizek, P. D. Hodgson, and H. Beladi, "Microstructure dependence of impact toughness in duplex stainless steels," *Materials Science and Engineering: A*, vol. 745, pp. 369–378, Feb. 2019. doi:10.1016/j.msea.2018.12.117
[81] J. Delgado, J. Ciurana, and C. A. Rodríguez, "Influence of process parameters on part quality and mechanical properties for DMLS and SLM with iron-based materials," *The International Journal of Advanced Manufacturing Technology*, vol. 60, no. 5–8, pp. 601–610, 2011. doi:10.1007/s00170-011-3643-5
[82] K. Kempen, E. Yasa, L. Thijs, J.-P. Kruth, and J. Van Humbeeck, "Microstructure and mechanical properties of selective laser melted 18ni-300 steel," *Physics Procedia*, vol. 12, pp. 255–263, 2011. doi:10.1016/j.phpro.2011.03.033
[83] H. Xiang, W. Zhao, and Y. Lu, "Effect of solution temperature on microstructure and mechanical properties of selective laser melted FE–22CR–5ni-0.26n duplex stainless steel," *Journal of Materials Research and Technology*, vol. 19, pp. 1379–1389, Jul. 2022. doi:10.1016/j.jmrt.2022.05.124

[84] K. Saeidi, L. Kevetkova, F. Lofaj, and Z. Shen, “Novel Ferritic stainless steel formed by laser melting from duplex stainless steel powder with advanced mechanical properties and high ductility,” *Materials Science and Engineering: A*, vol. 665, pp. 59–65, May 2016. doi:10.1016/j.msea.2016.04.027